STUDY OF DRY ICE GROWTH ON DUPLEX CYLINDERS

Pavlo Sokolov* **& Muhammad S.Virk**

Artic Technology & Icing Research Group, Institute of Industrial Technology, UiT – The Arctic University of Norway

* Address all correspondence to: Pavlo Sokolov, Artic Technology & Icing Research Group, Institute of Industrial Technology, UiT—The Arctic University of Norway, Lodve Langes Gate 2, 8514 Narvik, Norway Postboks 385, 8505 Narvik, E-mail: pavlo.sokolov@uit.no

Original Manuscript Submitted: 4/25/2022; Final Draft Received: 9/21/2022

ABSTRACT: *A study of dry ice growth on the bundled (duplex) cylinders has been performed using icing wind tunnel experiments and Computational Fluid Dynamics (CFD) numerical simulations. The aim of this study is to "fill the gaps" in the works of (Wagner, 2010) and (Qing et al., 2018). The numerical simulations cover a range of possible icing conditions by varying the operating wind speed, median volume diameter, and for some cases – the angle of incidence between the cylinders. The obtained results for the 0° AoA show that the accreted ice masses ratio between the leeward and windward cylinder varies from ~100% to ~30%. The accreted ice masses ratio decreases with the increase in the wind speed and/or median volume diameter. For the cases with non-zero AoA, the accreted ice masses become approximately equal, when the AoA is large enough to produce a vertical separation equal or greater to one cylinder diameter.*

KEY WORDS: *CFD, icing wind tunnel, ice accretion, droplet collision efficiency, cylinder, bundle*

1. INTRODUCTION

The study of atmospheric icing on power lines is a well-established field, with analytical models of power line icing specifically originating as early as 1980's (Makkonen, 1984). These models, in turn, are based on the theoretical work on atmospheric icing of structures, dating back to the works of Langmuir and Blodgett (1946) and other research, conducted at the Mt. Washington Observatory in the same timeframe. The resultant aggregated theoretical knowledge has been incorporated in the ISO 12494 standard "*Atmospheric Icing of Structures*". ISO 12494 modeling framework received widespread attention when it comes to the analytical modeling of ice accretion on simple geometries, which can be approximated by circular cylinder, such as simplex power line conductors, tubular telecommunication masts, etc.

Consequently, the modeling of atmospheric icing on structures with other geometrical configurations has received limited attention. One practical example of such a case is modeling of atmospheric icing on bundled conductors – duplex, triplex, hexa etc. bundled configurations. Such geometric configurations are of significant importance in the modeling of atmospheric icing on the overhead transmission lines, as the majority of high-voltage transmission networks consist of bundled conductors. However, to the best of authors' knowledge only limited amount of work has been done in modeling of atmospheric ice accretion on bundled cylinders and/or conductors, those primarily being the works of Wagner (2010) and Qing et al. (2018). Thus, there is a need to better understand such types of ice accretion and droplet impingement, although, it is not certain how or if ISO 12494 can handle the modeling of the atmospheric ice accretion on bundled conductors, nor how one could easily validate the obtained results.

Therefore, the use of Computational Fluid Dynamics (CFD) solvers is employed, which have been steadily increasing in popularity for the purposes of modeling atmospheric ice

accretion (Lozowski and Makkonen, 2005). The results of CFD modeling of atmospheric icing on structures have been extensively validated, primarily in the in-flight icing studies, for example, works by Papadakis et al. (2007), Ratvasky et al. (2008), Wiberg et al. (2014), etc. The setup of the numerical simulations, performed in this study, is aiming to represent the icing on the bundled conductors on typical power line under a range of possible icing conditions. For simplicity, the usage of circular cylinders is employed, and they are deemed an acceptable approximation to the actual stranded conductor with ribbed bare surface, especially after initial accretion smoothens the conductor surface.

2. PREVIOUS STUDIES

Recently, Qing et al. (2018) have performed a similar analysis of the rime ice accretion on bundled conductors, focusing primarily on the effect of the distance and separation angle on the rime ice accretion. However, the presentation of the results of their analysis leaves a few open questions.

Qing et al. specify that the turbulence model used in their analysis is standard k–ε model. Upon closer inspection it is apparent that the eq. (4) and the unnumbered equation after it in their paper is not a standard k–ε model but rather the Lam-Bremhorst (Lam and Bremhorst, 1981; Schmidt and Patankar, 1988) Low-Reynolds-number extension (LRN) to the k–ε model that employs a transport equation for the total dissipation rate, with the advantage that the model requires no additional source terms. However, a disadvantage of the Lam-Bremhorst model is that one of the damping functions requires the calculation of the local distance to the nearest wall. Qing et al. do not present the information about the mesh used in their paper, nor the y+ value of their setup is known.

Since neither the wall treatment nor the $y+$ values are known it poses some questions regarding applicability of their results for the modeling of the viscous sublayer in their CFD simulations. This matter is of importance as the droplets experience highest degrees of momentum change in the boundary layer near the wall. Another question what was the turbulence intensity used in the Qing et al. simulations as the LB LRN k–ε model has some potential issues with not predicting the turbulence transition for the turbulence intensities of an order of 1% and lower (Schmidt and Patankar, 1988). In addition, none of the k–ε models is implemented in the FENSAP–ICE. The importance of this point is discussed below.

For the discrete phase, Qing et al. present the mass and momentum conservation equations matching that of the FENSAP–ICE. Cross-referencing with the Fluent Theory Guide (ANSYS, 2017) shows that the discrete phase governing equations in the Fluent are different from the equations in the FENSAP–ICE/Qing et al. The usage of FENSAP–ICE is not mentioned in the source article (Qing et al., 2018). The authors specify that "*Numerical simulations were done by Fluent and MATLAB*." This makes of the nature of implementation of the discrete phase simulation in their work an open question.

Furthermore, an unnumbered equation immediately after the eq. (6) shows a peculiar definition of the drag coefficient C_D (original notation preserved):

$$C_D = \frac{0.44}{Re_w}$$

where "C_D *is the drag coefficient;* Re_w *is the droplets Reynold number;*". The authors of this work assume that this is the expression for the droplet drag coefficient. If this assumption is true, this formulation of the droplet drag coefficient differs significantly from the spherical droplet drag coefficients in the Fluent, FENSAP–ICE and analytical icing parameterizations models.

The inference of the analytical icing models is important at this step, as the droplet drag

parameterizations are in-built in the numerical CFD software packages and it would not be possible to easily change these in them, in order to investigate the potential impact of this peculiar droplet drag parameterization of Qing et al. on the resultant ice accretion. However, this is easily done for the droplet trajectories calculations method of Finstad (1986). Nonetheless, when discussing the numerical droplet drag parameterizations in the CFD software packages, for example, the FENSAP–ICE uses the following droplet drag coefficient expression (FENSAP–ICE User Manual):

$$C_D = (24/Re_d)\,(1 + 0.15Re_d^{0.687}) \qquad \text{for} \qquad Re_d \leq 1300$$

$$C_D = 0.4 \qquad \text{for} \qquad Re_d > 1300$$

where Re_d is the droplets Reynolds number. Fluent in the Discrete Phase Modeling (DPM) uses the droplet drag coefficient of Morsi and Alexander (1972) given as:

$$C_D = 24/Re_d \qquad \text{for} \qquad Re_d < 0.1$$

$$C_D = 22.73/Re_d + 0.0903/Re_d^2 + 3.69 \qquad \text{for} \qquad 0.1 < Re_d < 1$$

$$C_D = 29.1667/Re_d - 3.7778/Re_d^2 + 1.22 \qquad \text{for} \qquad 1 < Re_d < 10$$

$$C_D = 46.5/Re_d - 116.67/Re_d^2 + 0.6167 \qquad \text{for} \qquad 10 < Re_d < 100$$

$$C_D = 98.33/Re_d - 2778/Re_d^2 + 0.3644 \qquad \text{for} \qquad 100 < Re_d < 1000$$

$$C_D = 148.62/\mathrm{Re_d} - 4.75\times10^4/\mathrm{Re_d}^2 + 0.357 \qquad \text{for} \qquad 1000 < Re_d < 5000$$

$$C_D = -490.546/Re_d - 57.87\times10^4/Re_d^2 + 0.46 \qquad \text{for} \qquad 5000 < Re_d < 10000$$

$$C_D = -1662.5/Re_d - 5.4167\times10^6/Re_d^2 + 0.5191 \qquad \text{for} \qquad 10000 < Re_d < 50000$$

Finstad in her doctoral thesis (Finstad, 1986) uses the droplet drag coefficients of Beard and Pruppacher (1969) and Langmuir and Blodgett (1946). These droplet drag coefficients are given as (Finstad, 1986):

$$(C_D Re/24) = 1 + 0.102Re^{0.955} \qquad \text{for} \qquad 0.2 \leq Re_d \leq 2.0$$

$$(C_D Re/24) = 1 + 0.115 Re^{0.802} \quad \text{for} \quad 2.0 \le Re_d \le 21.0$$

$$(C_D Re/24) = 1 + 0.189 Re^{0.632} \quad \text{for} \quad 21.0 \le Re_d \le 200.0$$

$$(C_D Re/24) = 1 + 0.197 Re^{0.63} + 2.6 \times 10^{-4} Re^{1.38} \quad \text{for} \quad 200 < Re_d$$

where the last parameterization is the droplet drag coefficient of Langmuir and Blodgett (1946) which they apply for the full range of droplet's Reynolds number Re_d.

Essentially, it makes the droplet trajectories, when calculated with the Qing et al. expression for the droplet drag coefficient almost a straight line, as in the absence of a significant drag, acting on the droplet, the inertia dominates the droplet motion. Fig. 1 illustrates this concept. The droplet trajectories in Fig. 1 are obtained from the code, replicated from the Finstad's Ph.D. thesis (Finstad, 1986). The code's performance was validated against the experimental data of Makkonen and Stallabrass (1987). The operating conditions in the trajectory calculations are identical to the ones in Table 1 in Qing et al. (2018). The only difference is the droplet drag coefficient parameterization used— Qing et al. vs. Beard and Pruppacher (1969), as implemented by Finstad herself in the original code.The droplet's staring coordinates (x_0, y_0) are $(-10R, 1/3R)$, where R is the cylinder radius.

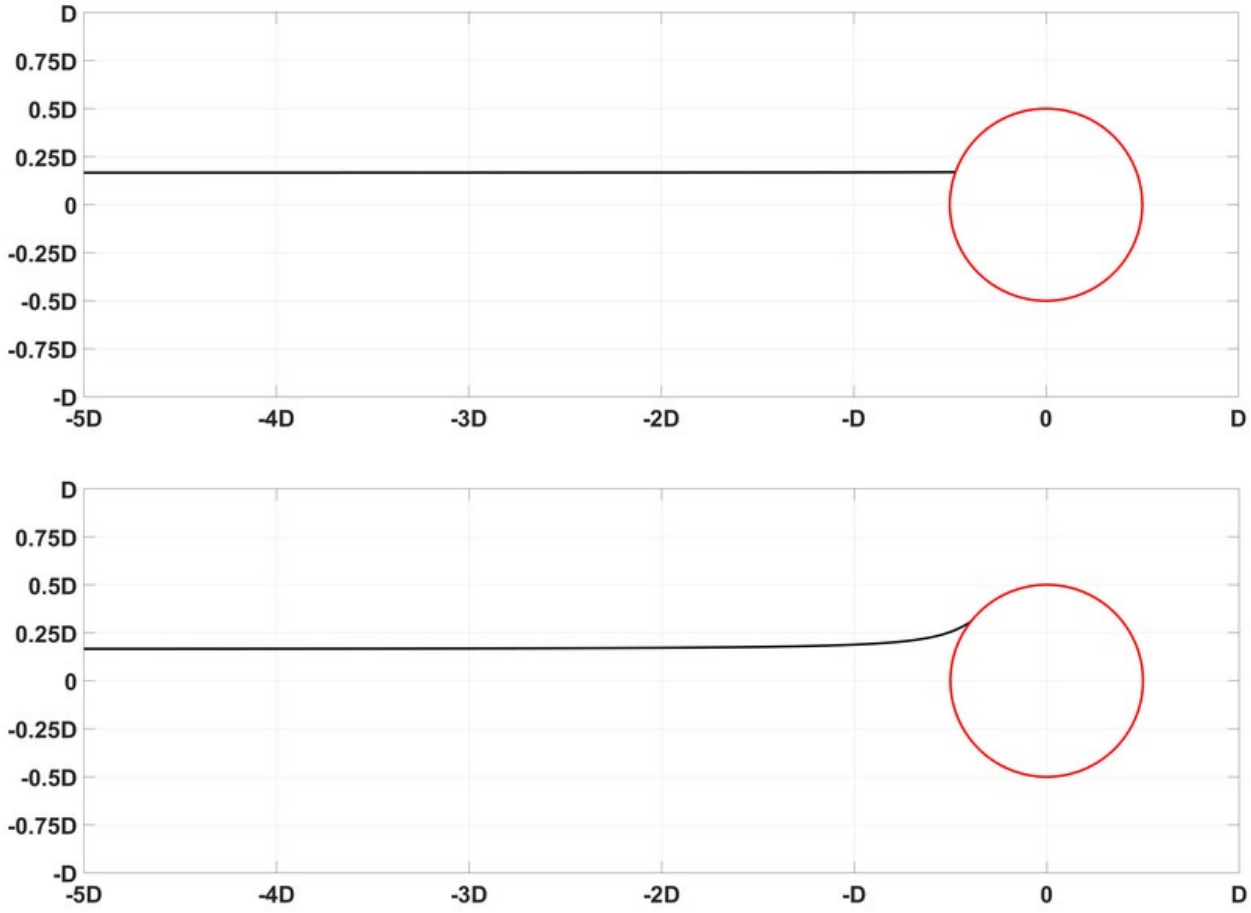

FIG. 1: Droplet trajectories obtained using the Qing et al. (2018) droplet drag coefficient (top) and Beard and Pruppacher drag coefficient (1969) (bottom)

The resultant overall collision efficiencies obtained from the trajectory calculations for this case are E = 0.37 with Beard and Pruppacher droplet drag coefficient, and E = 0.97 with Qing et al. droplet drag coefficient. The ISO 12494 (ISO, 2001) overall collision efficiency formula gives for this particular case the overall collision efficiency E = 0.37. Furthermore, reverse calculating the overall collision efficiencies from Tables 2 and 3 in Qing et al. (2018) for the windward conductor at the same operating condition yields the consistent value of the overall collision efficiency of E = 0.34. Such discrepancy between the obtained analytical results and the presented simulation results is puzzling.

Another major work focusing on the ice accretion on the bundled conductors in the Ph.D. thesis of Wagner (2010). In their work, for the dispersed phase, Wagner uses their own code, which is a Lagrangian particle tracking approach, based on the application of Newton's Second Law, with the total force F, acting on the particle being the sum of drag, buoyancy and gravity forces. The trajectories equations are solved using Runge-Kutta fourth and fifth order algorithm. For the droplet drag coefficient, Wagner uses the following fit to the droplet drag coefficient of Langmuir and Blodgett:

$$C_D = (24/Re_d)\left(1 - 0.391Re_d^{0.3289} + 0.5648Re_d^{0.4561}\right) \quad \text{for} \quad 0 < Re_d \leq 10$$

$$C_D = (24/Re_d)\left(1 + 0.1767Re_d^{0.6536}\right) \quad \text{for} \quad 10 < Re_d \leq 200$$

$$C_D = (24/Re_d)\left(4 + 0.01052Re_d^{1.048}\right) \quad \text{for} \quad 200 < Re_d$$

Similarly, the droplet drag coefficient by Wagner (2010) performs well in the trajectory calculations, using the analytical code from Finstad (1986). The value of the overall collision efficiency obtained with this coefficient is E = 0.36, which is very close to the value of the overall collision efficiency E = 0.37, obtained by using ISO 12494 formulae and the unmodified Finstad code. The example of droplet trajectory calculations is given in Fig. 2, with the same operating and initial conditions as in Fig. 1.

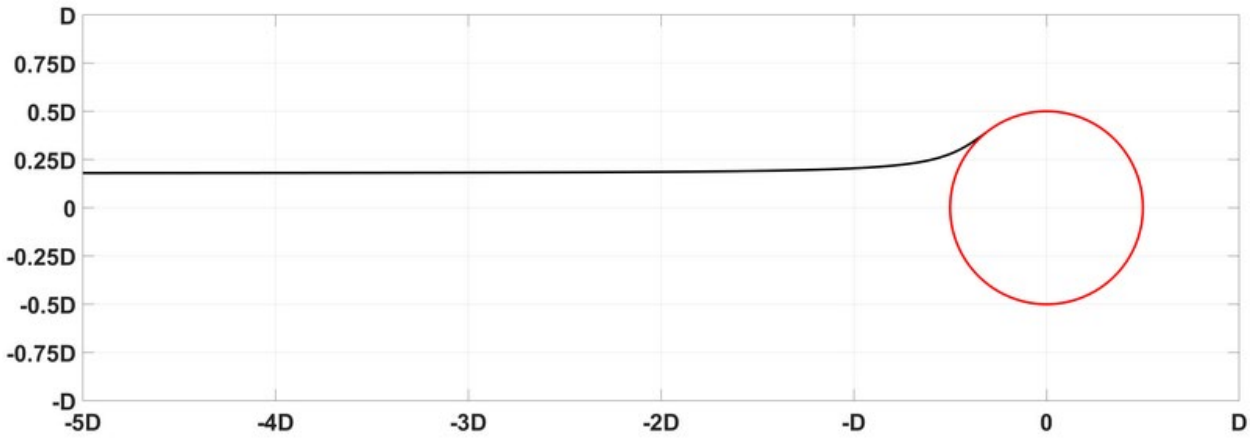

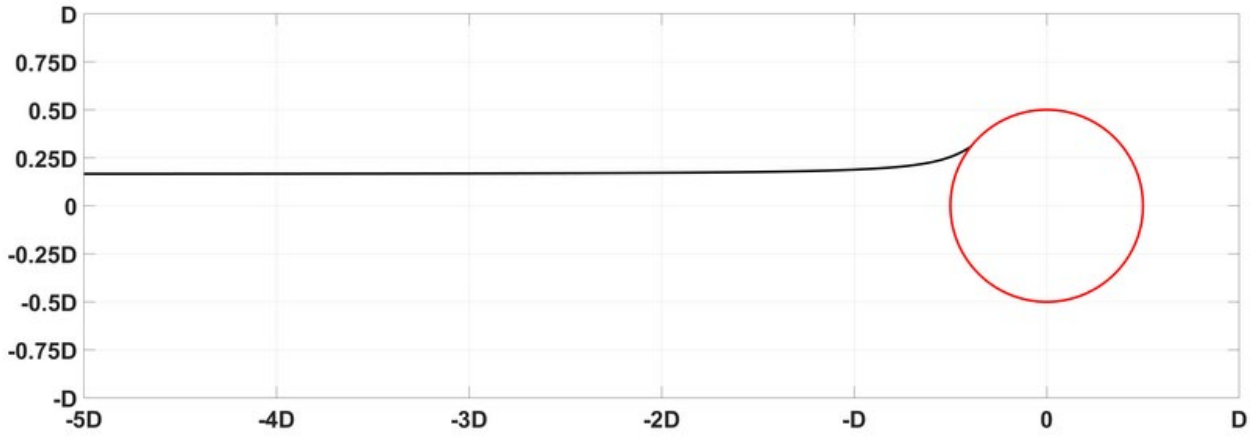

FIG. 2: Droplet trajectories obtained using the Wagner droplet drag coefficient (top) and Beard and Pruppacher drag coefficient (bottom)

In graphical form, the comparison of all aforementioned droplet drag coefficient parameterizations is given in Fig. 3 for the droplets Reynolds number range $0 < Re_d < 100$, which is believed to cover the majority of typical icing conditions.

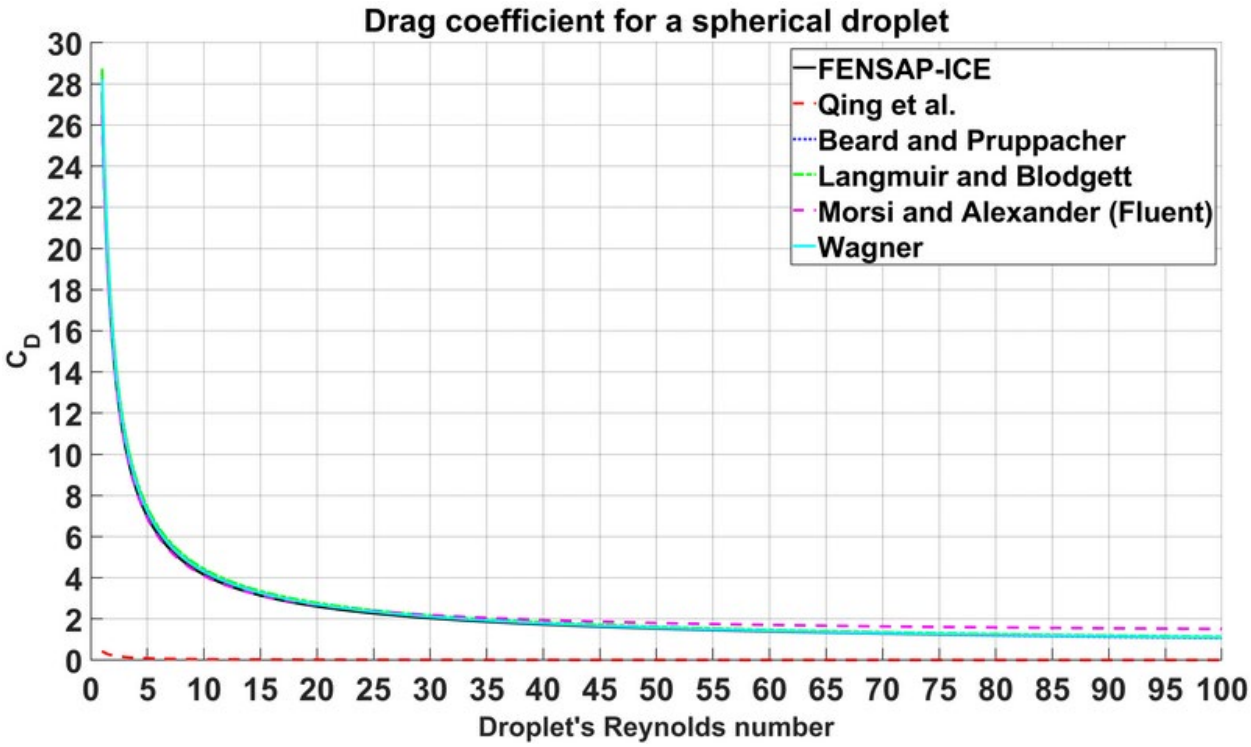

FIG. 3: Droplet drag coefficient *CD* for a spherical droplet as a function of droplet's Reynolds number Re_d

As it can be seen from Fig. 3 nearly all droplet drag coefficient parameterizations have a good agreement among each other for the entire range of droplet's Reynolds number. All, but the one presented in Qing et al. (2018), which gives the results of $C_D < 1$ for $Re_d > 0.44$, along with $C_D \rightarrow 0$ as droplet's Reynolds number increases. It is unknown where Qing et al. (2018) have obtained this expression for the spherical droplet drag coefficient. It is not present in references of Bourgault et al. (1999) and Fluent (2006), associated with the governing equations for the droplet motion in their paper.

In addition, Qing et al. write (original notation preserved): "*Due to wind, air and super-cooled water droplets move with respect to the conductor. While air bypasses the conductor, water droplets collide onto the conductor because of their inertia, as shown in Fig. 1. The local collision efficiency is then defined as follows:*

$$\alpha_1 = \mathrm{d}y/\mathrm{d}L$$

where α_1 is the local collision efficiency, dy is the ordinate difference of two starting points, and dL is the distance along the conductor between two impact points." This statement is followed by: "*The flow of air and water droplets follows the principle of fluid mechanics and can be regarded as gas-liquid twophase flow. Here, the Euler's model was used to analyze the two-phase flow (Bourgault et al., 1999). In this model, both air and water droplets are treated as continuous phase, and the volume of one phase cannot be occupied by the other. By establishing the governing equations for each phase, the characteristic of flow field can be calculated*."

Such definition of local collision efficiency is consistent with the descriptions of Finstad (1986) and Finstad et al (1988). However, such definition of the local collision efficiency is valid

for the Lagrangian approach and not Eulerian approach. Since Eulerian approach does not track individual particles such definition of local collision efficiency makes no sense. For example, the FENSAP–ICE, which is an Eulerian solver, defines the local collision efficiency as (FENSAP–ICE User Manual):

$$\beta = -\frac{\alpha \overrightarrow{V_d} \cdot \vec{n}}{w V_\infty} \tag{1}$$

where α is the local volume fraction (kg/m^3), w is the Liquid Water Content (LWC), V_∞ is a freestream wind speed and $\vec{n}$ is the surface normal vector. The overall collision efficiency is then calculated as the integration of local collision efficiencies over surface area and is given as:

$$\beta_{tot} = \frac{\int \beta \, \mathrm{d}A}{L_\infty^2} \tag{2}$$

The integral is normalized by a characteristic length L_∞.

Furthermore, since the cloud impingement parameters, i.e., the overall and local collision efficiencies, impact velocities and maximum impingement angles are all coupled with each other and depend on the droplet inertia parameter K and the Langmuir parameter φ as it can be seen from the equations and discussion in Finstad (1986) and Finstad et al. (1988), an overestimation of one of them, e.g. the overall collision efficiency, in an analytical calculations will result in an overestimation of the rest of them. Since Qing et al. use the local collision efficiency definition given by Finstad (1986) and Finstad et al. (1988), and as it was shown previously – the trajectory calculations with their droplet drag coefficient overestimate the overall collision efficiency significantly, it will also result in serious overestimation of the local collision efficiencies.

This presents a question – how did Qing et al. actually carry out their analysis? The combination of purely Lagrangian definition of the local collision efficiency with statements regarding an Eulerian approach for multiphase flow, along with mixing together governing

equations from both Fluent and FENAP–ICE is challenging to reconcile within the scope of one model. Was Fluent predominantly used and coupled with FENSAP–ICE? Or vice-versa? To what extent the numerical simulations were performed in Matlab? And what was the setup of them? Was the Fluent DPM used? These questions make their simulation setup nigh impossible to replicate and validate the data in this work against it.

Wagner (2010) has used a standard k–ε model with Launder–Sharma values for constants $C_{\varepsilon 1}$, $C_{\varepsilon 2}$, σ_k and σ_ε. Since their $y+$ values are in the range of $30 \leq y+ \leq 300$ the usage of the logarithmic wall function is implemented. The choice of the standard k–ε model was governed by, quoting Wagner (2010): "*Other turbulence models may overestimate the extension of the wake and therefore its effect on the ice accretion, like the k–ω model for instance. Hence, the chosen approach is on the safe side, which is beneficial for investigating whether there is an effect of tandem arrangement of conductors on the ice accretion or not*." They also note a few shortcomings to their fluid dynamics model, in particular, applied wall model does not account for adverse pressure gradients in the boundary layer, meaning that the pressure decreases in flow direction. In addition, the near wake, is significantly underestimated and the separation angle is overestimated, compared to the experiment (Wagner, 2010). The flow field simulations are performed in COMSOL in their study.

Finally, in their parametric study Wagner focuses on the effects of the wind speed, Median Volume Diameter (MVD), conductor temperature etc. on the wet and dry ice formation. Unfortunately, the parametric study on the characteristics of icing of bundled conductors is limited in their work. The only practical conclusion in their parametric study was classifying the ice accretion on bundled cylinders as "full", "partial" and "no ice accretion".

Unfortunately, Wagner did not attempt to quantify the "full", "partial" and "no ice

accretion on downstream conductor" further in their work, unlike Qing et al. (2018), which present the accreted ice masses. Although, as it was discussed previously, the authors of this work have certain reservations towards the results in Qing et al. (2018). Out of presented conclusions in their work, the authors of this study have confidence in two of them. First, being the increase in the angle of incidence between the conductors in the bundle "normalizing" the ice accretion on bundled conductors. The smallest angle (Qing et al., 2018) tested was 30° at 400 mm separation, which gives the vertical separation of 200 mm, or, alternatively ten conductor diameters. Second being "*at a distance of more than 1000 mm the influence on the leeward conductor by the windward conductor becomes very small*." Such horizontal separation to conductor diameter ratio (L/D) = 50 makes any sort of wake effects perturbing the airflow around the leeward conductor highly unlikely, unlike the horizontal separation to conductor ratio of Wagner (2010), being equal to 10.

Thus in order to perform a meaningful study and to "fill the knowledge gaps" between the works of Wagner (2010) and Qing et al. (2018) the choice of operating conditions should be "in between" these two works, in order to not replicate one or both of the studies. The aggregated operating conditions in Wagner (2010) and Qing et al. (2018) are given in Table 1.

TABLE 1: Summary of operating conditions in Wagner (2010) and Qing et al. (2018)

Wagner	
Wind speed (m/s)	5 – 15
Droplet size (μm)	0 – 140
Conductor diameter (mm)	40
Conductor length (m)	Unspecified
Horizontal separation (mm)	400
Vertical separation (°)	0, 0.96, 1.91, 2.86
Liquid Water Content (g/m^3)	Unspecified, assumed to be 1.2, based on information in the same section.
Operating temperature (°C)	Unspecified, assumed to be –5, based on the same reasoning as

	above.
Icing duration (min)	Unspecified
Qing et al., Simulation	
Wind speed (m/s)	10
Droplet size (μm)	20 (MVD)
Conductor diameter (mm)	20
Conductor length (m)	1
Horizontal separation (mm)	200, 400, 600, 800, 1000
Vertical separation (°)	0, 30, 40, 60, 90 (at a total separation of 400 mm)
Liquid Water Content (g/m^3)	0.5
Operating temperature (°C)	–10
Icing duration (min)	30
Qing et al., Experiment	
Wind speed (m/s)	10, 20
Droplet size (μm)	19 (MVD)
Conductor diameter (mm)	30
Conductor length (m)	0.5
Horizontal separation (mm)	200, 300, 400, 600, 940
Vertical separation (°)	–
Liquid Water Content (g/m^3)	0.5
Operating temperature (°C)	–5
Icing duration (min)	30

Furthermore, two additional goals are deemed to be worth investigating within the scope of this study. First, is an attempt to "expand" the work by Wagner (2010), by presenting the accreted ice mass ratios for the simulations within this study, in attempt to further quantify the "partial ice accretion on downstream conductor" statement. Second, is to ascertain the viability of the commercial CFD package in the modeling of the dry ice accretion on the bundled conductor, as opposed to creating the in-house code. If such ice accretions can be viably modeled by a commercial CFD software, then it would be readily possible to extend this work further, in an attempt to produce the accreted ice masses ratio between the windward and the leeward conductor as a function of the operating conditions. Finally, it is worth mentioning that icing of bundled conductors receives recent attention in the field of atmospheric icing, with Veerakumar et al. (2022) conducting an experimental measurement of drag forces on iced bundles. However,

since their focus was on the aerodynamic drag and not on quantifying accreted ice masses ratio, their work will receive limited attention in this study, with some measurement results being used for validation purposes.

3. DESIGN OF THE EXPERIMENT

Table 2 shows the operating conditions in this study with Fig. 4 giving a schematic overview of the duplex bundled cylinders setup.

TABLE 2: Operating conditions

Parameter	Value
Cylinder diameter (mm)	30
Air velocity (m/s)	4, 7, 10, 20
Air temperature. (°C)	–5
Altitude (m.a.g.l)	10
Median Volume Diameter (μm)	15, 20, 25, 30, 40
Liquid Water Content (g/m^3)	0.4
Icing duration (min)	30
Cylinder separation (mm)	500
Droplet distribution spectrum	Monodisperse

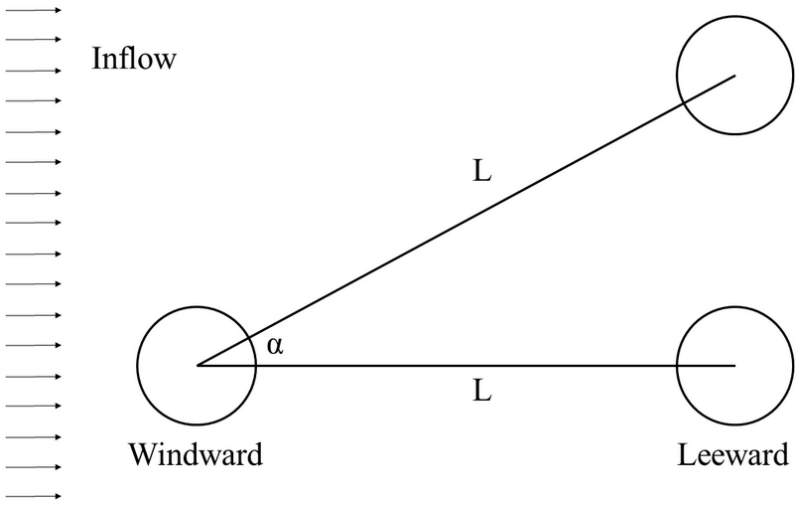

FIG. 4: Schematic overview

The choice of cylinder diameter and separation is deemed to be representative of an actual diameter and separation of a typical duplex conductor bundle. This is based on personal communications with Prof. Jiang Xingliang, (Chongqing University, China), and EFLA, Iceland. In both countries, the separation of ~30 mm conductors in a bundle is equal to 450 – 470 mm. The range of air velocities in this study is deemed representative of simulating in-cloud icing in typical conditions, and the choice of Median Volume Diameters (MVDs) should also be sufficient to represent the naturally occurring variation, without going into the Supercooled Large Droplet (SLD) size ranges, thus introducing potential issues with splashing and bouncing of the droplets.

Furthermore, the case of a cylinder bundle being exposed to icing at operating wind speed of 10 m/s and MVD of 20 μm was selected for further investigation of the effect of an angle/vertical separation on the icing on bundled conductors. The vertical separations chosen are one cylinder radius (15 mm; ~1.7° angle), one cylinder diameter (30 mm; ~3.4°), two cylinder diameters (60 mm, ~6.8°) and 129.4 mm, corresponding to the angle of 15° exactly. This range of vertical separations fits in between the simulation cases, performed at different angle by Wagner (2010) and Qing et al. (2018). The reason for performing numerical simulations at different angles is to simulate the gradual sag of the conductor bundle (1.7° – 6.8° angles) and extreme sag due to significant ice accretion (15° angle). Larger angles are not considered in this study as its assumed that the leeward conductor would not be “shielded” by a windward one past this point and thus the flow conditions and the ice accretion on both of them would be almost identical, as covered by Qing et al. (2018).

Finally, in order to streamline the subsequent analysis some assumptions and

simplifications have been made in this study. First, the assumption of "dry ice growth", i.e., all droplets stick and freeze on impact, and that the temperature of –5° C is sufficient for this. Second, is the choice of using the monodisperse distribution for modeling purpose. The reason for this is two-fold – to keep the obtained results "in compliance" with the ISO 12494 framework; and to avoid any potential discrepancies the usage of droplet distribution spectrum can introduce on the leeward cylinder, i.e., as the different bins in the distribution will have different overall collision efficiencies, MVD and Liquid Water Content (LWC) values along with the possibility that actual droplet distribution spectrum can be different from the windward cylinder, thus increasing the number of potential variables in the analysis.

3.1 Numerical Setup

The multiphase CFD based numerical simulations were carried out using ANSYS FENSAP-ICE, which uses Eulerian water droplet impingement solver. The existing analytical models of droplet behavior such as Langmuir and Blodgett (1946), Finstad et al. (1988) etc. solve droplet trajectories using Lagrangian particle tracking approach. The Eulerian method treats the particle phase as a continuum and develops its conservation equations on a control volume basis and in a similar form as that for the fluid phase. The Lagrangian method considers particles as a discrete phase and tracks the pathway of each individual particle. By studying the statistics of particle trajectories, the Lagrangian method is also able to calculate the particle concentration and other phase data. On the other hand, by studying particle velocity vectors and its magnitudes in Eulerian method, it is possible to reconstruct the pathways and trajectories of particles in a phase. From the pathways, trajectories and the impingement locations of the supercooled liquid droplets one can reconstruct the dry growth ice accretion as follows. For an example "static" (no forced

and/or free rotation) circular cylinder under dry growth conditions the distribution of local collision efficiencies β would yield the end accreted ice shape and ice mass, ignoring the sublimation and/or evaporation. There are two reasons for this. First, for the dry ice growth, by definition, $\alpha_2 = \alpha_3 = 1$, meaning both the sticking (α_2) and the freezing (α_3) efficiencies are both equal to unity. Thus, it follows that no accreted ice mass is lost due to water runback (α_3) or bouncing off the surface (α_2). Next, geometrically, the local collision efficiency can be defined as

$$\beta = \frac{\mathrm{d}y}{\mathrm{d}l} \tag{3}$$

where dy is the initial vertical separation of the droplet (with respect of the axis of symmetry, y = 0) and dl is the computed vertical separation on the object's surface, with respect to some point L, which would be the impact location, if the droplet trajectory was a straight line. Thus, it follows that $\mathrm{d}l > l$, and consequently, $\beta < 1$, or $\mathrm{d}l = l$, and $\beta = 1$ (a prominent effect in the trajectory model of Finstad for the stagnation line collision efficiency β_0 only). Thus, by tracking the initial droplet coordinates (x_0, y_0) and the droplet impact coordinates (x_f, y_f) one can estimate the distribution of the local collision efficiencies and the accreted ice shape. Following that, the accreted ice mass can be obtained using the overall collision efficiency (α_1). The overall collision efficiency, α1, in a geometric sense can be defined as the value of the initial vertical separation y' of a droplet, at the given MVD, which yields a "grazing" trajectory (meaning all other droplets, with the same diameter, starting from some position $y_s > y'$ will not collide with the object), divided by the characteristic length of the object (in this example of a circular cylinder, the characteristic length is the cylinder radius). With the value of the overall collision efficiency α1 known, the accreted ice mass can be estimated using the "Makkonen model" as:

$$\frac{\mathrm{d}M}{\mathrm{d}t} = \alpha_1 v A w t \tag{4}$$

where M is the accreted ice mass (in g), v is the operating wind speed (in m/s), w is LWC (g/m^3), t is the exposure time (s) and A is the cross-sectional area with respect to the normal direction of the incoming flow (m^2; in this cylinder example $A = DL$, where D is the cylinder diameter and L is the cylinder length, both in m). Do note the omission of α_2 and α_3 terms from the "Makkonen model" above, as again. for the dry growth, $\alpha_2 = \alpha_3 = 1$.

However, do not that this discussion applies for the analytical trajectory model of Finstad, and by extension, same principles hold for the Lagrangian approach. Since the FENSAP-ICE is an Eulerian solver, the definition of local and overall collision efficiencies is different. They are estimated as shown by the eqs. (1) and (2) in this work. Moreover, when it comes to the boundary condition for the liquid phase on the stationary wall, the particle transport equations of DROP3D are hyperbolic and they only need conditions to be defined at upstream boundaries. Inflow nodes are assigned Dirichlet conditions for particle properties, while walls and exits are free. Particles leave the computational domain through walls as water catch and exits. Similar to losing total air pressure through screens, particle concentration is also reduced across these boundaries as a function of the local blockage and water catch on the screens (FENSAP–ICE User Manual).

When it comes to the choice of working within the Eulerian or Lagrangian framework, one has to think about applicability of a given tool to the problem in question, and to what specific purposes said tool(s) was/were developed. FENSAP-ICE is an Eulerian flow field only solver. While the authors of the FENSAP-ICE do not explicitly mention the reasons which governed their choice, some logical deductions can be made. First, it is a common way to treat the incoming air flow in the CFD solvers as continuum phase. For this purpose, the Eulerian specification is a common and customary choice. Second, the FENSAP-ICE was primarily

developed for the purpose of studying the atmospheric icing in the aerospace industry, primarily, fixed-wing aircraft and rotorcraft icing. In such operating conditions, one expects to operate with high values of the droplet inertia - i.e., the trajectories of all, bar the smallest supercooled water droplets do not deviate from straight-line trajectories by a significant amount. Only close to the object itself, on the characteristic distances of an order of mm or so, one can expect to find some sort of curvature to the trajectories. Thus, the need for more computationally demanding calculation procedure, such as the Lagrangian particle tracking is questionable. Last, the FENSAP-ICE User Manual explicitly mentions that "The air and particle equations could be solved simultaneously (as in a two-phase flow). However, since the density of a water droplet is 1,000 times greater than the density of air and the water fraction is dilute, the equations are solved in a segregated manner. The airflow is solved first, followed by the particle equations. In other words, the effect of the air on the particle is considered, but not the reverse." This makes sense, as the impingement solver, also written to the Eulerian specification, would be easier to couple with the airflow field solver, also written in the Eulerian frame.

On the other hand, consider the analytical trajectory calculations of Finstad, also referenced in this work. Finstad employs a Lagrangian approach in her doctoral work. However, the problem Finstad was studying is a bit different problem, compared to what the FENSAP-ICE was developed to solve. For aerospace segment, the most important "features" of an icing event to consider is the resultant ice accretion after exposure, how it degrades the aerodynamic performance, evaluation of possible anti- and de-icing solution and validation of ice shapes for certification purposes. While Finstad was interested in the re-evaluation of the droplet trajectories on “more modern machine” in order to improve the at the time existing analytical models of droplet impingement. Since the focus of Finstad was the impingement characteristics,

studying individual droplet trajectories and their deviations was critical. Thus, employing the Langrangian flow specification for the droplets was a natural choice. However, it came with a cost of the "physical accuracy" of the air flow field specification, for which a potential flow approximation was used - i.e., an inviscid and irrotational flow field. While Finstad did carry a comparison with the experimental ice shapes, for the purposes of model's validation, they were not the main objective. Furthermore, consider how many potential supercooled droplets there are within a cloud, as for example, the Weather Research Forecast (WRF) model use the cloud condensation nuclei value of 100 per cm^3 which is equal 10^8 nuclei per m^3, when compared to trajectory analysis of Finstad (of max 7000 droplet trajectories in the original work, being the doctoral thesis of Finstad).

Detailed mesh sensitivity analysis were carried out to accurately determine the boundary layer characteristics (shear stress and heat fluxes), a $y+$ values of less than 1 is used near the cylinder wall surface. Number of mesh elements and $y+$ value was selected based upon the heat flux calculations, where a numerical check was imposed that the heat flux computed with the classical formulae dT/dn should be comparable with the heat flux computed with the Gresho's method.

The calculation of $y+$ value is performed in the following way (White, 2002):

$$Re = \frac{\rho_f U_\infty L_\infty}{\mu_f} \tag{5}$$

$$C_f = \frac{0.026}{Re^{1/7}} \tag{6}$$

$$\tau_{wall} = \frac{C_f \rho_f U_\infty^2}{2} \tag{7}$$

$$U_{fric} = \sqrt{\frac{\tau_{wall}}{\rho_f}} \tag{8}$$

$$\Delta s = \frac{y^{+}\mu_{\mathrm{f}}}{U_{fric}\rho_{\mathrm{f}}} \tag{9}$$

where ρ_{f} and μ_{f} are the density and dynamic viscosity of the continuous phase (air), U_{∞} is the freestream velocity, L_{∞} is the characteristic length, i.e., cylinder diameter, C_f is the skin friction coefficient, τ_{wall} is the shear stress at the wall, U_{fric} is the friction velocity and Δs is the wall spacing (first cell height). These computations are based on the flat-plate boundary layer theory from White (2002). Based on the highest operating wind speed in the Table 2 being equal to 20 m/s, this gives the $\Delta s = 12.2\times10^{-6}$ m for $y+ = 1$. Thus, the first cell height used in the meshes in this study, and being equal to $\Delta s = 1\times10^{-6}$ m yields a $y+$ value of $y+ = 0.08$ for the highest freestream wind speed value of 20 m/s.

The computational mesh used for all CFD simulations at 0° incidence is a hybrid mesh, consisting of structured quad elements near the cylinders and the unstructured tri elements elsewhere. The first cell height at both cylinders is 1×10^{-6} m with exponential growth factor of 1.1 and a total of 100 inflation layers. In addition, the length of the cylinder "wall" itself is divided into a 100 nodes. This results in 30000 structured quad elements per cylinder (since FENSAP–ICE is exclusively a 3D solver, a three cell extrusion in z-direction is used), for a total of 60000 structured quad elements. The rest of the mesh is filled with unstructured tri mesh, for a total cell count of 105960 cells in the computational domain. Furthermore, fine quad and tri elements were used in cylinder wake region, whereas coarse tri elements were used for the rest of the outer domain. The computational mesh is also shown in Fig. 5.

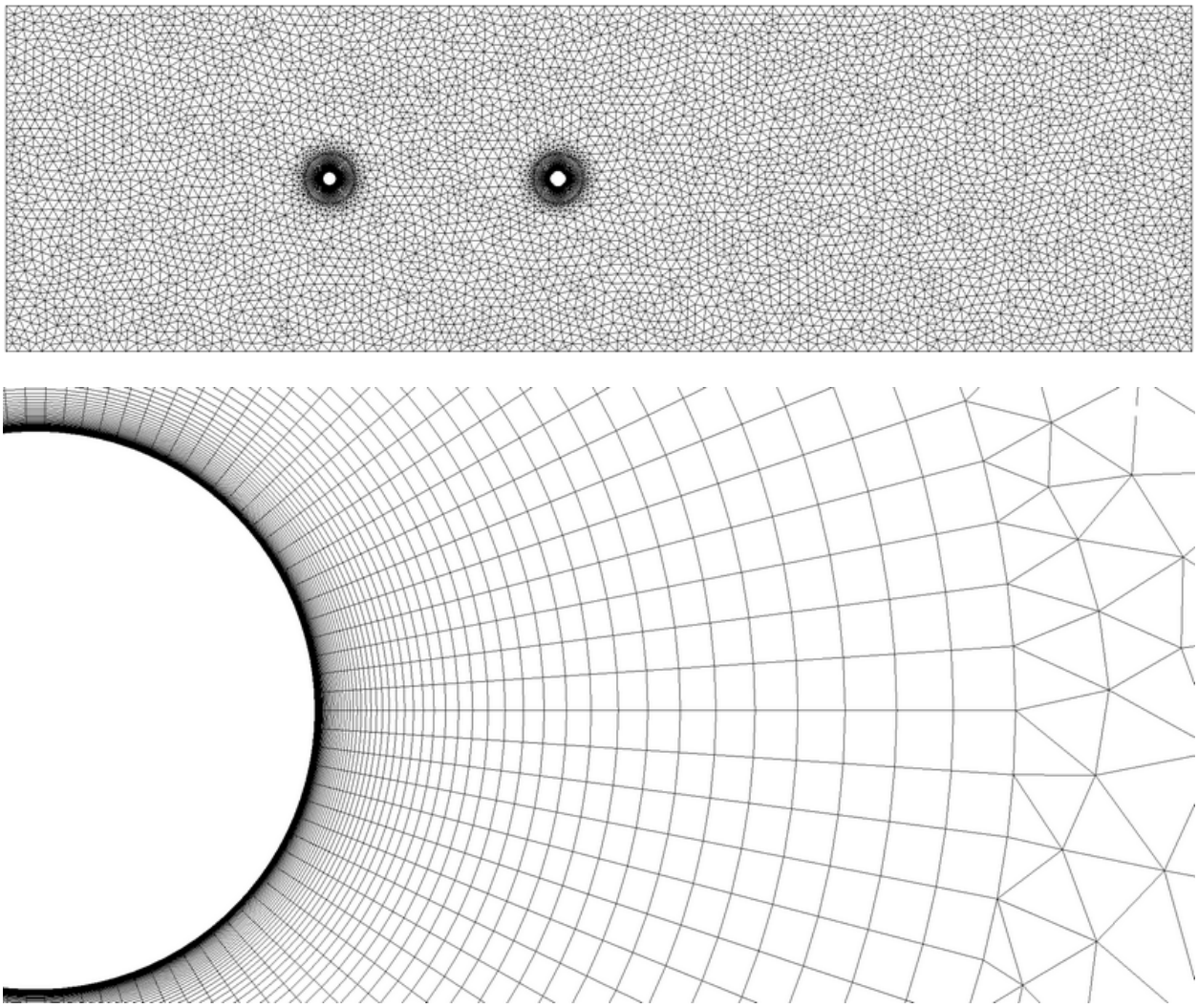

FIG. 5: Computational mesh. Bottom image shows the closeup of the windward cylinder wake region.

The turbulence model chosen for this study is a *k*–ω Shear Stress Transport (SST) model (Menter, 1992). This choice is governed by a few factors. First, in authors opinion, this model is the best option for this particular type of modeling, when considering other available turbulence models in FENSAP–ICE, those being laminar, Spalart-Allmaras, and LRN *k*–ω model (FENSAP–ICE User Manual). Second, is to test the hypothesis of Wagner (2010) of the potential overestimate of wake extension of *k*–ω models and their impact on the resultant ice accretion. Third, is to test the performance of the *k*–ω SST model itself for this type of atmospheric ice

modeling, as the *k*–ω SST is a widely used turbulence model, which combines the robustness of *k*–ω model in near-wall and boundary layer region with the reliability of *k*–ε model in the farfield region. Last, is to ascertain, if the dry ice accretion of the bundled conductors can be carried within the constraints of one commercial CFD package, without coupling the solution procedure to other CFD packages, e.g. Fluent or the in-house code. While we do present the results for the steady-state solution, all steady-state simulations were performed at CFL 1 (lowest possible value for the Ansys Fensap–ICE).

While this work deals with the dry ice growth only, for posterity purposes, the details of the thermodynamic model of FENSAP-ICE will be given. ICE3D solves a system of two partial differential equations on all solid surfaces. The first equation expresses mass conservation:

$$\rho_f \left[\frac{\partial h_f}{\partial t} + \vec{\nabla} \cdot \left(\overline{V}_f h_f \right) \right] = V_\infty LWC\beta - \dot{m}_{evap} - \dot{m}_{ice} \tag{10}$$

where the three terms on the right hand side correspond, respectively, to the mass transfer by water droplet impingement (source for the film), by evaporation and by ice accretion (sinks for the film).

The second partial differential equation expresses conservation of energy:

$$\rho_f \left[\frac{\partial h_f c_f \tilde{T}_f}{\partial t} + \vec{\nabla} \cdot \left(\overline{V}_f h_f c_f \tilde{T}_f \right) \right] = \left[c_f \left(\tilde{T}_\infty - \tilde{T}_f \right) + \frac{\left\| \vec{V}_d \right\|^2}{2} \right] V_\infty LWC\beta - L_{evap} \dot{m}_{evap}$$

$$+ \left(L_{fusion} - c_s \tilde{T} \right) \dot{m}_{ice} + \sigma\varepsilon \left(T_\infty^4 - T_f^4 \right) - c_h \left(\tilde{T}_f - \tilde{T}_{ice,rec} \right) + Q_{anti\text{-}icing} \tag{11}$$

where the first three terms on the right hand side model the heat transfer generated by the impinging supercooled water droplets, by evaporation and by ice accretion. The last three terms are the radiative, convective and 1D conductive heat fluxes.

The coefficients ρ_f, c_f, c_s, σ, ε, k_s, L_{evap}, L_{fusion} are physical properties of the fluid and of

the solid, specified by the user. The reference conditions T_∞, V_∞, LWC are airflow and droplets parameters specified by the user. The local wall shear stress τ_{wall} and the convective heat flux Q_h should be supplied by the flow solver, while the DROP3D module provides local values of the collection efficiency β and droplets impact velocity V_d.

The evaporative mass m_{evap} flux is recovered from the convective heat flux, using a parametric model. $Q_{anti\text{-}icing}$ is the anti-icing heat flux obtained from C3D module for wet air calculations. Three unknowns remain to be computed: the film thickness h_f, the equilibrium temperature T_f at the air/water film/ice/wall interface and the instantaneous mass accumulation of ice m_{ice}. Compatibility relations are needed to close the system of equations. Based on physical observations, one way to write them is as follows:

$$\begin{cases} h_f \geq 0 \\ \dot{m}_{ice} \geq 0 \\ h_f \tilde{T}_f \geq 0 \\ \dot{m}_{ice} \tilde{T}_f \leq 0 \end{cases}$$

These inequalities ensure that the model predicts no liquid water when the equilibrium temperature is below the freezing point (0˚C), and that no ice forms if there is film that is above 0˚C.

The same thermodynamic model holds true for both wet and dry ice growth, however, for the dry ice growth there is considerably less emphasis on the heat transfer, in practice, as by definition of dry ice growth all droplets immediately freeze on impact. This is a combination of several phenomena, resulting from the choice of operating conditions. Namely, low operating temperature, considerably below the freezing point, results in very light droplets freezing almost instantaneously, which coupled with low wind speeds, means that the effect aerodynamic heating can be ignored. In addition, the combination of MVD, LWC, operating and impact velocities results in a fact that any heat supplied to the wall by latent heat released due to solidification of

droplets can also largely be ignored. Furthermore, the kinetic heating due to the impinging droplets can de disregarded due to very low kinetic energies being carried by impinging droplets, by virtue of their extremely small masses and low impact velocities (which are a fraction of operating wind speed). Finally, and most importantly, both in simulations (and in experiments) the cylinders are unheated so there is no external heat source in the system. For the purposes of "sanity check" the ICE3D output log was studied after each simulation in order to check for water presence film, which shouldn't be present in dry ice growth. No simulation logs showed any trace of liquid water film being present in the CFD simulations.

4. RESULTS AND DISCUSSION

From the physics perspective, the modeling of the atmospheric ice accretion on bundled cylinders presents more challenge when compared to the single cylinder. The ice accretion of single cylinders can be adequately modeled analytically by the inviscid, potential flow approximation (Langmuir and Blodgett, 1946; Finstad, 1986), with later model being experimentally verified by Makkonen and Stallabrass (1987) for the range of overall collision efficiencies of $0.07 < E < 0.63$. In the modeling of ice accretion on single conductors there is no value in modeling droplet trajectories past the cylinder as the most important characteristic of it – collision with cylinder or miss will already be determined.

For bundled configuration this is insufficient, as the information about the droplet not colliding with the windward cylinder is insufficient to determine whether or not the droplet in question will collide with the leeward cylinder. Thus, recovering the state of the multiphase flow past the windward conductor is of primary importance for modeling of the ice accretion of the bundled cylinders. Both the airflow solution, primarily the airflow velocity components, and the

droplet behavior, such as, establishing the droplets velocity components, inertia and drag have to be obtained. The problem is exacerbated by the fact that, in practice, the majority of icing events are expected to happen at cylinder Reynolds number in the range of 10^4 – 10^5, resulting in a turbulent flow. Thus, such features of the turbulent, viscous flow as turbulent wake, vorticity, vorticity shedding, oscillations, boundary layer response etc. might be of importance, as they can affect the airflow and droplet behavior. An example of multiphase flow solution from the CFD simulations in this study is presented in Figs. 6 and 7 showing the droplet velocity magnitudes and LWC distributions respectively, for some selected cases from Table 2.

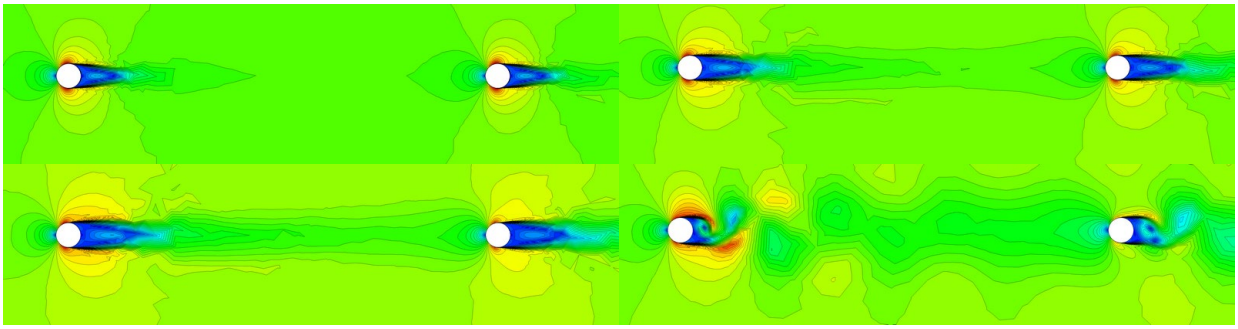

FIG. 6: Air velocity magnitudes in CFD simulations. The operating conditions are V = 4 m/s (top left); V = 7 m/s, (top right); V = 10 m/s (bottom left); and V = 20 m/s (bottom right).

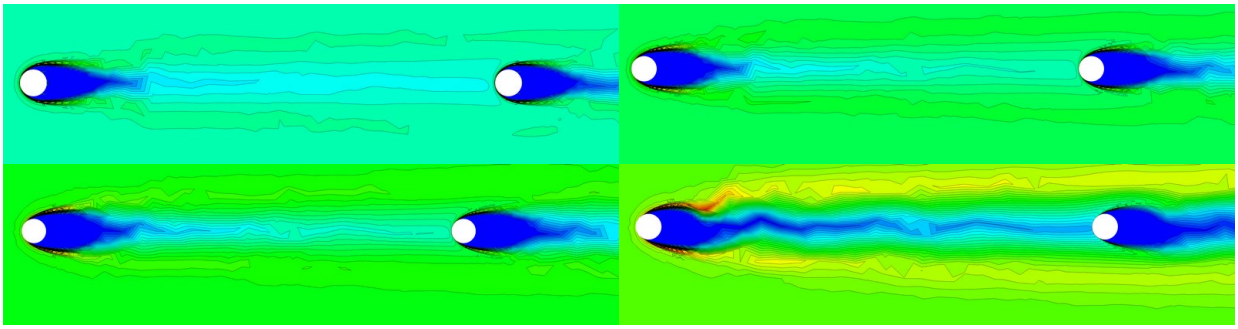

FIG. 7: Liquid water content distributions in CFD simulations. The operating conditions are V = 4 m/s (top left); V = 7 m/s, (top right); V = 10 m/s (bottom left); and V = 20 m/s (bottom right). MVD = 25 μm for all cases.

Tables 3 and 4 show the overall collision efficiencies (*E*) and their ratios between the windward and the leeward cylinders respectively for all test cases from Table 2.

TABLE 3: Overall collision efficiencies on the windward (W) and leeward (L) cylinders

MVD / V	15		20		25		30		40	
	W	**L**	**W**	**L**	**W**	**L**	**W**	**L**	**W**	**L**
4	0.005	0.007	0.057	0.054	0.140	0.122	0.224	0.186	0.371	0.277
7	0.052	0.045	0.154	0.122	0.256	0.193	0.347	0.242	0.490	0.298
10	0.103	0.077	0.223	0.150	0.330	0.204	0.421	0.238	0.557	0.278
20	0.233	0.095	0.372	0.139	0.479	0.163	0.563	0.181	0.679	0.209

TABLE 4: Overall collision efficiencies ratios of leeward to windward cylinders

MVD / V	15	20	25	30	40
4	121%	94%	87%	83%	75%
7	87%	79%	75%	70%	61%
10	75%	67%	62%	57%	50%
20	41%	37%	34%	32%	31%

Since for the “dry growth” regime the sticking and freezing efficiencies, $\alpha_2 = \alpha_3 = 1$ respectively, the accreted ice mass ratios between the windward and the leeward cylinders will be identical to overall collision efficiencies ratios from Table 4. Visually, the ratio from Table 4 is given in Fig. 8. For the dry ice growth, the overall collision efficiencies ratio will also be equal to the accreted ice masses ratio.

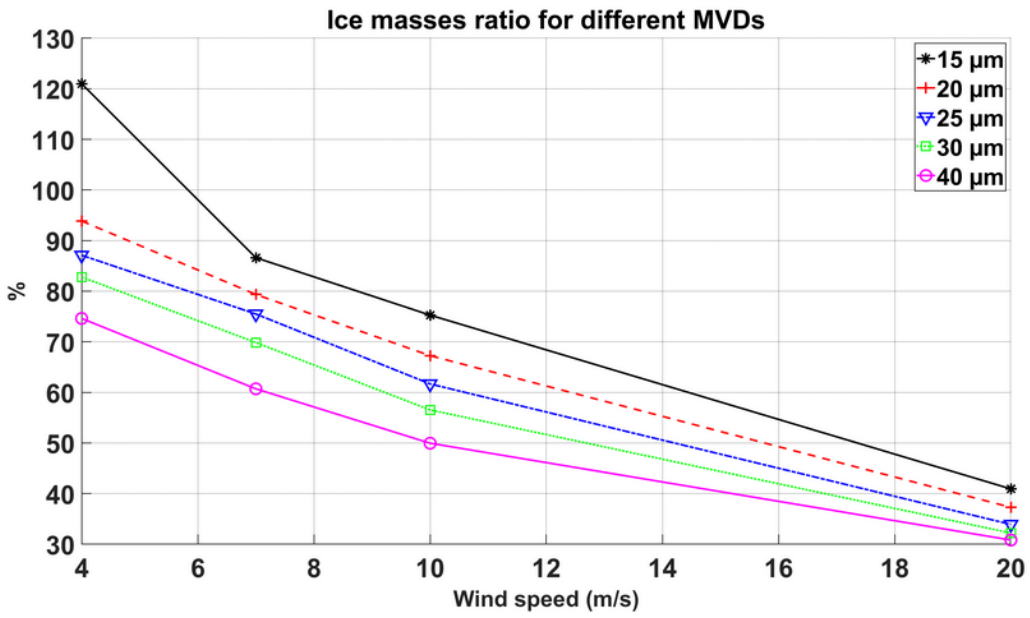

FIG. 8: Overall collision efficiencies for bundled cylinders in this study

From Table 3 and Fig. 8 the conclusion that can be made is that with the increase in the MVD and/or wind speed values, the ratio overall collision efficiencies between the leeward and the windward cylinder decreases from "full accretion" to a "partial accretion" of an around 31%. The decrease in the overall collision efficiencies is more "steeper" for smaller MVDs. This decrease can be directly correlated to the increase in the droplet's inertia parameter K, and to lesser extent – the Langmuir parameter φ. These parameters are obtained as:

$$K = \frac{\rho_p d_p^2 V}{9\mu_f D} \tag{12}$$

$$\varphi = \frac{Re^2}{K} = \frac{9\rho_f{}^2 DV}{\mu_f \rho_p} \tag{13}$$

where d_p is droplet diameter, D is the cylinder diameter, V is the wind speed, ρ and μ are density and dynamic viscosity, respectively with subscripts f and p referring to fluid and particle, respectively. From the operating conditions in Table 1 the values of cylinder diameter,

separation, particle and fluid densities and viscosities are constant, thus it follows that any variance in ice mass ratios in Table 3 must be explainable as a function of K, which depends on the value of product Vd_p^2 and φ which depends on the wind speed alone (granted, both of the aforementioned products also depend on the cylinder diameter D, however, in this study this value is constant).

The physical explanation behind the decrease of the accreted ice mass ratios, associated with the increase in values of K and φ is two-fold. First, with the increase of droplet's inertia, associated with the increase of MVD and/or wind speed, the inertia will be dominating the droplet movement and thus the characteristic time for the droplet to adapt to the new conditions will increase. For example, the increase in the wind speed will result in shorter "time window" for the droplet, passing over the windward cylinder, to adjust to new trajectory, such that allows for the collision with the leeward cylinder, at a given separation. In addition, higher wind speeds result in the wake effects being prominent, potentially affecting the ice accretion of the leeward conductor as it can be inferred from Fig. 6.

For completeness purposes, the values of droplet inertia parameter K and Langmuir parameter φ for the test cases in this study are given in Table 5.

TABLE 5: Values of droplet inertia parameter K and Langmuir parameter φ for the bundled cylinders

MVD / V	15		20		25		30		40	
	K	**φ**	***K***	**φ**	***K***	**φ**	***K***	**φ**	***K***	**φ**
4	0.19	110	0.35	110	0.54	110	0.78	110	1.38	110
7	0.34	192	0.61	192	0.95	192	1.36	192	2.42	192
10	0.49	274	0.87	274	1.35	274	1.95	274	3.46	274
20	0.97	548	1.73	548	2.70	548	3.89	548	6.92	548

For the values of $K < 0.25$ (Finstad et al., 1988) advise to "*recalculate the droplet trajectories using the appropriate drag coefficients for each droplet size in the spectra*." The FENSAP–ICE uses the following expression for the droplet's continuity and momentum equations:

$$\frac{\partial \alpha}{\partial t} + \vec{\nabla} \cdot \left(\alpha \overrightarrow{V_d}\right) = 0 \tag{14}$$

$$\underbrace{\frac{\partial \left(\alpha \overrightarrow{V_d}\right)}{\partial t} + \vec{\nabla}\left[\alpha \overrightarrow{V_d} \otimes \overrightarrow{V_d}\right]}_{\text{I}} = \underbrace{\frac{C_D Re_d}{24K} \alpha \left(\overrightarrow{V_a} - \overrightarrow{V_d}\right)}_{\text{II}} + \underbrace{\alpha \left(1 - \frac{\rho_a}{\rho_d}\right) \frac{1}{Fr^2}}_{\text{III}} \tag{15}$$

where the variables α and $V_{d,a}$ are mean field values of, respectively, the water volume fraction and droplet velocity.

The terms of this equation are, respectively, the:

- I – material derivative of acceleration.
- II – (steady-state) drag action the droplets of mean diameter *d*.
- III – buoyancy and the gravity forces.

As such, FENSAP–ICE lacks the term pertaining to the calculation of the "history term", which for the cases of $K < 0.25$ can make significant difference, when it comes to the overall collision efficiencies, as discussed in Finstad et al. (1988). As such, the "physical meaning" of the simulation results at $V = 4$ m/s and MVD = 15 μm, which results in the accreted ice masses ratio of 121% can be questioned.

Furthermore, Fig. 9 shows the overall collision efficiencies ratio from Table 4 compared to the value of the droplet inertia parameter *K*.

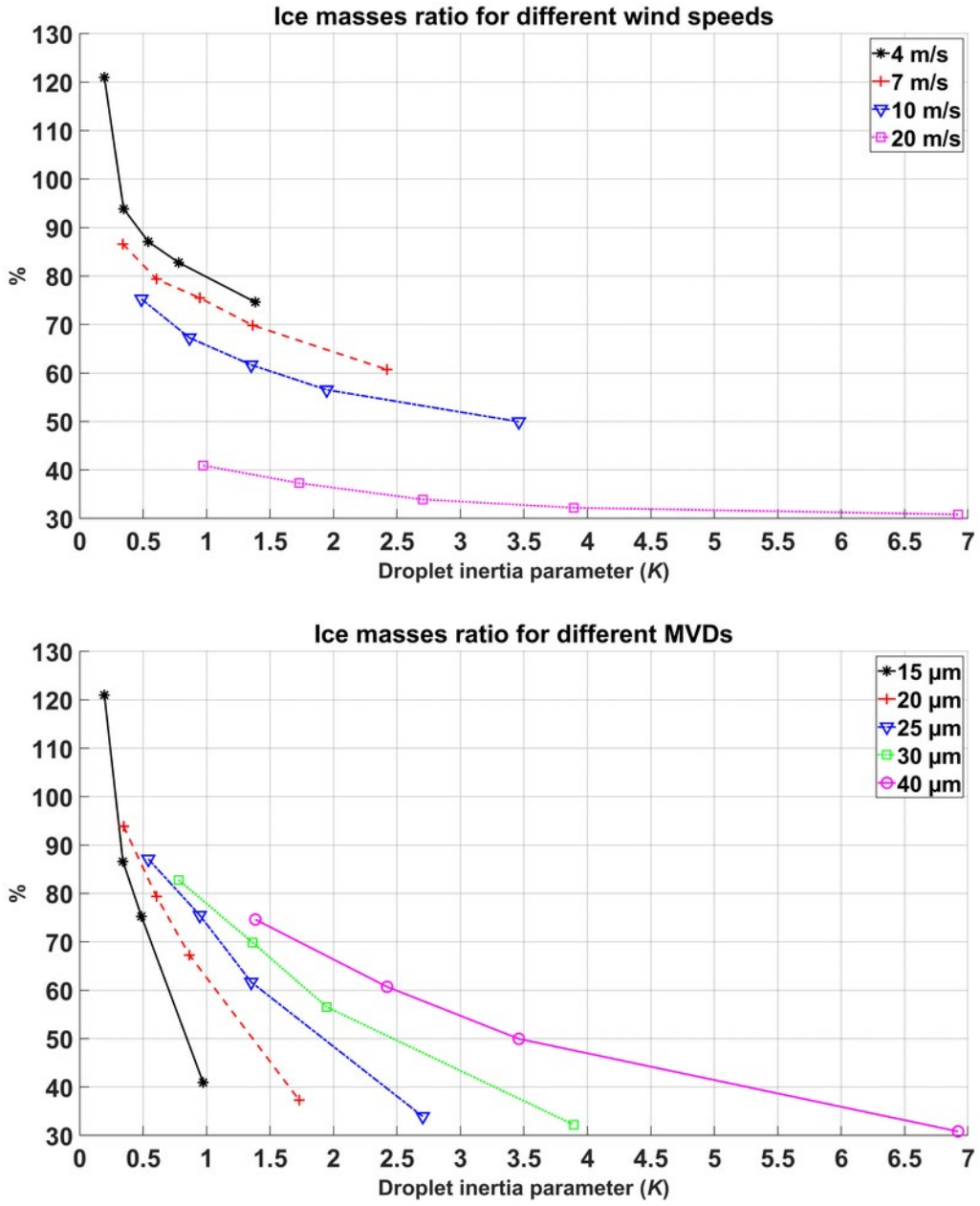

FIG. 9: Accreted ice masses ratio vs. droplet inertia parameter K for different wind speeds (top) and MVDs (bottom). Each marker in the plot corresponds to one pair of wind speed and MVD from Table 4.

Fig. 9 shows that the accreted ice masses ratio decreases in the similar fashion for all combinations of wind speeds and/or MVDs with the increase in the value of K. Moreover, the curves, featuring inherent larger changes in values of K, for example, at 4 m/s wind speed or at

MVD of 15 μm tend to decrease the accreted ice masses ratio faster. This is in agreement with the results of (Wagner, 2010), as shown in their thesis, especially for the curve dividing "full" and "partial" accretion, as in that plot the higher values of K are towards upper right of the plot. Unfortunately, it is not possible to quantify the results further, as Wagner (2010) haven't presented the overall collision efficiencies or the accreted ice masses ratios in their work. The authors of the current work do not think they are at the liberty to attempt to quantify what Wagner constitute as "full", "partial" and "no ice accretion" on the windward and leeward conductors in their work. The only available information about that in their work is this classification, and thus the direct comparison of the results is not possible without making fundamental assumptions towards Wagner's work.

In addition, an interesting point in the results from Table 4 and Fig. 9 is a rapid drop in the accreted ice masses ratio at the 20 m/s wind speed, for all tested MVDs, when compared to the results at 4 – 10 m/s wind speed. From Figs. 6 and 7 it can be seen that the wake behavior changes significantly at 20 m/s, with the significant vortex shedding present in the wake. When comparing the airflow behavior in the wake for the results in Wagner (2010) and the references contained within, for the flow at $Re = 4.5\times10^4$ (for the 20 m/s operating conditions in this study, the cylinder Reynolds number is $Re = 4.6\times10^4$), the wake length is larger and the relative velocities in the wake are lower in this work. These effects of the wake on the leeward cylinder, coupled with the possible entrainment of droplets in the vortices, can explain the sudden drop of the accreted ice masses ratio at 20 m/s operating wind speed.

There are a few potential explanations of this result. First, is the overestimation of the wake in the k – ω turbulence model, as suggested by Wagner. However, as evidenced by the PIV measurements of Veerakumar et al. (2022) of iced conductors at $Re = 5\times10^4$ the velocity

distribution and its recovery in the wake zone may be underestimated, in turn, in the results of Wagner. The primary differences are the extent of the recirculation zone, which is larger in the experiments of Veerakumar et al. (2022) and the rate of horizontal velocity increase in the wake, which is again, higher in the results of Veerakumar et al. Figure 10 shows the comparison of Veerakumar et al. experimental measurements and the Wagner simulations.

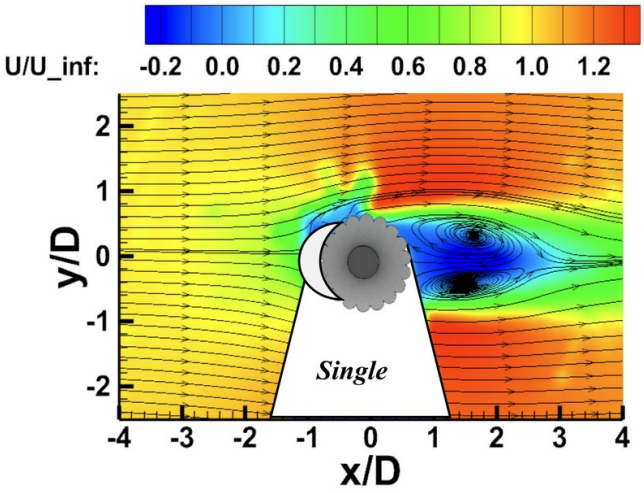

FIG. 10: Horizontal velocity distribution in the wake in Veerakumar et al. measurements

As the experimental measurements of Veerakumar et al. were performed on the 29 mm conductor, compared to the 30 mm conductor in this work, it was deemed by the authors of this work that the 1 mm difference in the characteristic dimension would not make too much difference on the results, in terms of Reynolds number. Thus, the computational mesh from the Fig.5 was reused for the purposes of validation with the Veerakumar et al. data. The primary reason is the consistency in the grids used in this work. The rest of operating conditions were selected as is presented by Veerakumar et al. Since the horizontal velocity distribution from Fig. 10 deals with the airflow only and not the multiphase flow, the validation was conducted using

the airflow simulations only. Figure 11 shows the droplet velocity vectors for the conditions of Veerkakumar et al. Note, that in this work and in Wagner the *L*/*D* ratio of 10 is chosen, while in Veerakumar et al. the closest reference point is *L*/*D* of 12 for the cylinder separation distance.

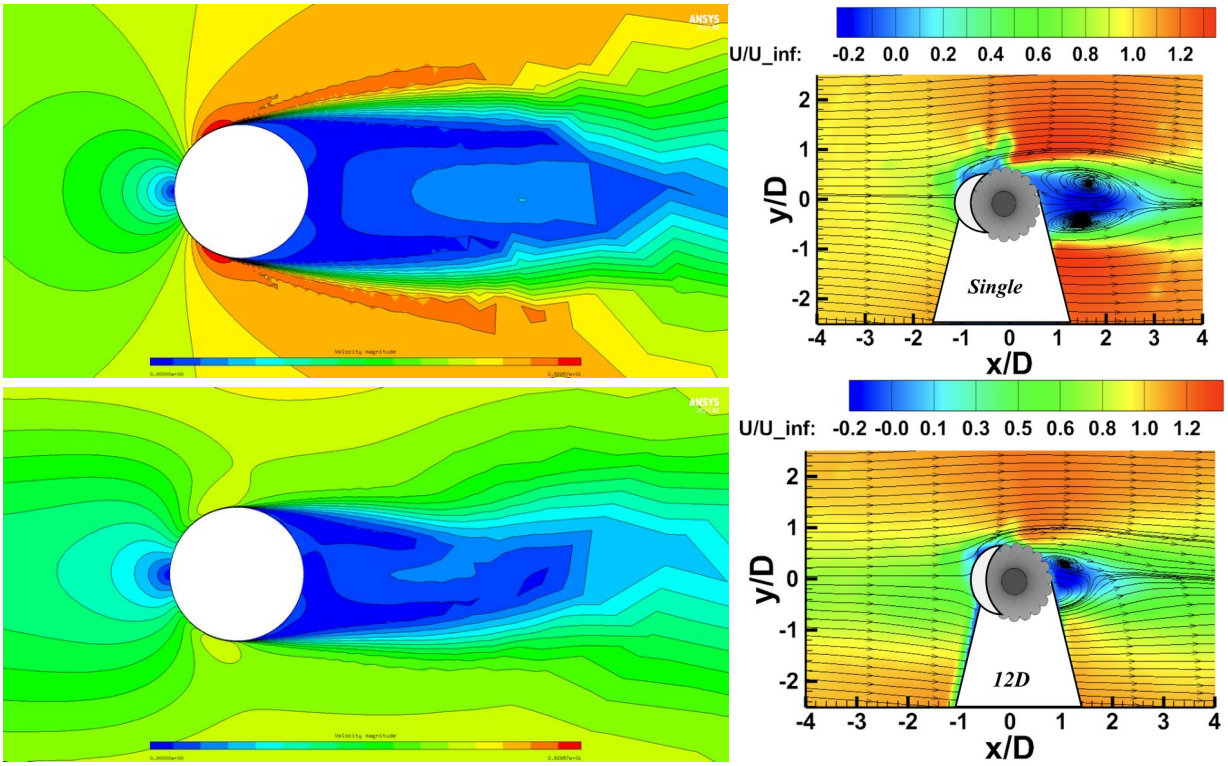

FIG. 11: Velocity distributions around the windward (top row) and leeward (bottom row) conductors. Results from this work (left) and Veerakumar et al. (right).

Figure 11 shows that the velocity distributions and the extent of recirculation zones agree well between the results of this work and the PIV measurements of the Veerakumar et al. The agreement between the numerical simulations and the experimental data is deemed sufficient, although the wake of the leeward conductor in the CFD simulations is overestimated compared to the experimental data. However, for the purposes of studying the accreted ice masses ratio in the duplex configuration this effect is of a little importance.

Furthermore, Fig. 12 shows the comparison of the centerline horizontal wind velocity in the numerical simulations between this work and the results of Wagner at matching *Re* values, those being $Re = 1.5\times10^4$ and $Re = 4.5\times10^4$.

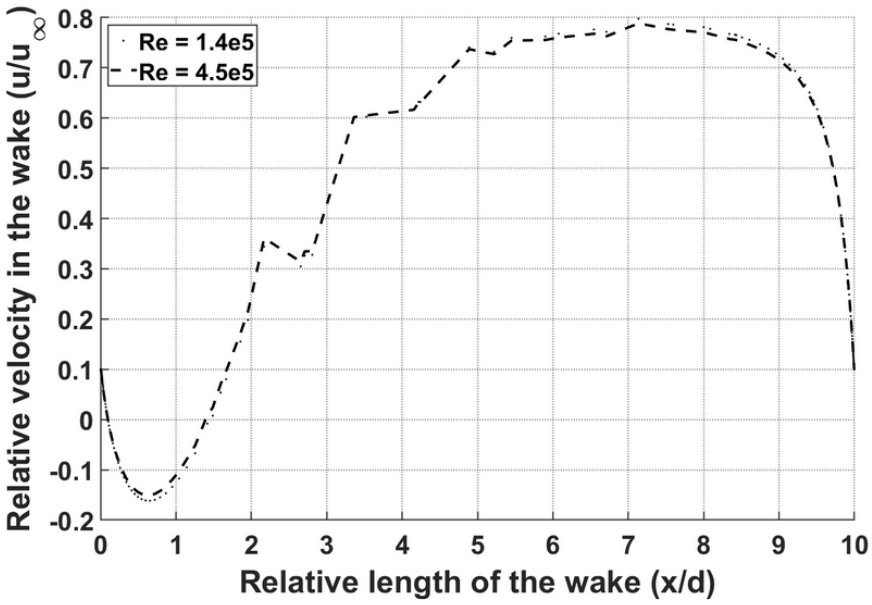

FIG. 12: Horizontal velocity distribution in the wake

From Fig. 12 it can be seen that at a further away distance from the windward cylinder, corresponding to the *x*/*d* distance of four, the agreement between the results of this work and Wagner's is good. However, at closer distances the difference in the relative wake velocities are large. In case of the Wagner, the extent of the recirculation zone is limited to $x/d = 0.37$ (Wagner, 2010), while in this work, its quite larger, approximately equal to the $x/d = 1.5$, which lines up well with the PIV measurements by Veerakumar et al.

When it comes to the change in the overall collision efficiencies between the windward and the leeward cylinders, the increase of the overall collision efficiency values on the leeward conductor will not scale linearly with the corresponding increase of the overall collision on the

windward conductor. As per Finstad et al. (1988), the general expression for the calculation of the overall collision efficiency α_1, stagnation line impact velocity V_0 and collision efficiency β_0 and the maximum impingement angle θ is:

$$\begin{aligned} X(K,\phi) = \left[C_{X,1}K^{C_{X,2}}\exp\left(C_{X,3}K^{C_{X,4}}\right) + C_{X,5}\right] - \left[C_{X,6}(\phi - 100)^{C_{X,7}}\right] \times \\ \times\left[C_{X,8}K^{C_{X,9}}\exp\left(C_{X,10}K^{C_{X,11}}\right) + C_{X,12}\right] \end{aligned} \quad (16)$$

with the value of constants $C_1 - C_{12}$ available in the original source (Finstad et al., 1988). This equation has a non-linear dependence on the values of the of cloud impingement parameters, primarily the overall collision efficiency, on K and φ values.

FENSAP–ICE estimates the accreted ice mass in a similar way to ISO 12494 as:

$$M = \alpha_1\alpha_2\alpha_3 wVAt \quad (17)$$

where w is the liquid water content, α_1, α_2 and α_3 are the non-dimensional collision, sticking and freezing efficiencies respectively, t is the icing duration and A is the surface area of the object. The only difference between the FENSAP–ICE and the ISO 12494 estimation of the accreted ice mass is in the value of the area A. The FENSAP–ICE uses the surface area of an object while ISO 12494 uses the $A = DL$ expression for a circular cylinder where D is the diameter and L is the cylinder length. For the case of a circular cylinder, it is simple to account for the difference in the area used and thus the accreted ice masses for bundled cylinders in this study are given in Table 6.

TABLE 6: Accreted ice masses on the windward (W) and leeward (L) cylinders. Values are in g/m

MVD / V	15		20		25		30		40	
	W	**L**	**W**	**L**	**W**	**L**	**W**	**L**	**W**	**L**
4	0.5	0.6	5.0	4.7	12.1	10.5	19.4	16.0	32.0	23.9
7	7.9	6.8	23.3	18.5	38.7	29.2	52.4	36.6	74.2	45.0

10	22.2	16.7	48.1	32.4	71.3	44.0	90.8	51.4	120.3	60.1
20	100.6	41.2	160.5	59.9	207.0	70.2	243.0	78.3	293.4	90.4

Fig. 13 shows the accreted ice masses for all operating conditions in this study plotted against the droplet inertia parameter *K*. In addition, a curve has been added, corresponding to the analytical calculations for the accreted ice mass on the windward conductor, carried out using ISO 12494 formulae/trajectories calculation method. The value of the droplet inertia parameter *K* was estimated from the eq. (8).

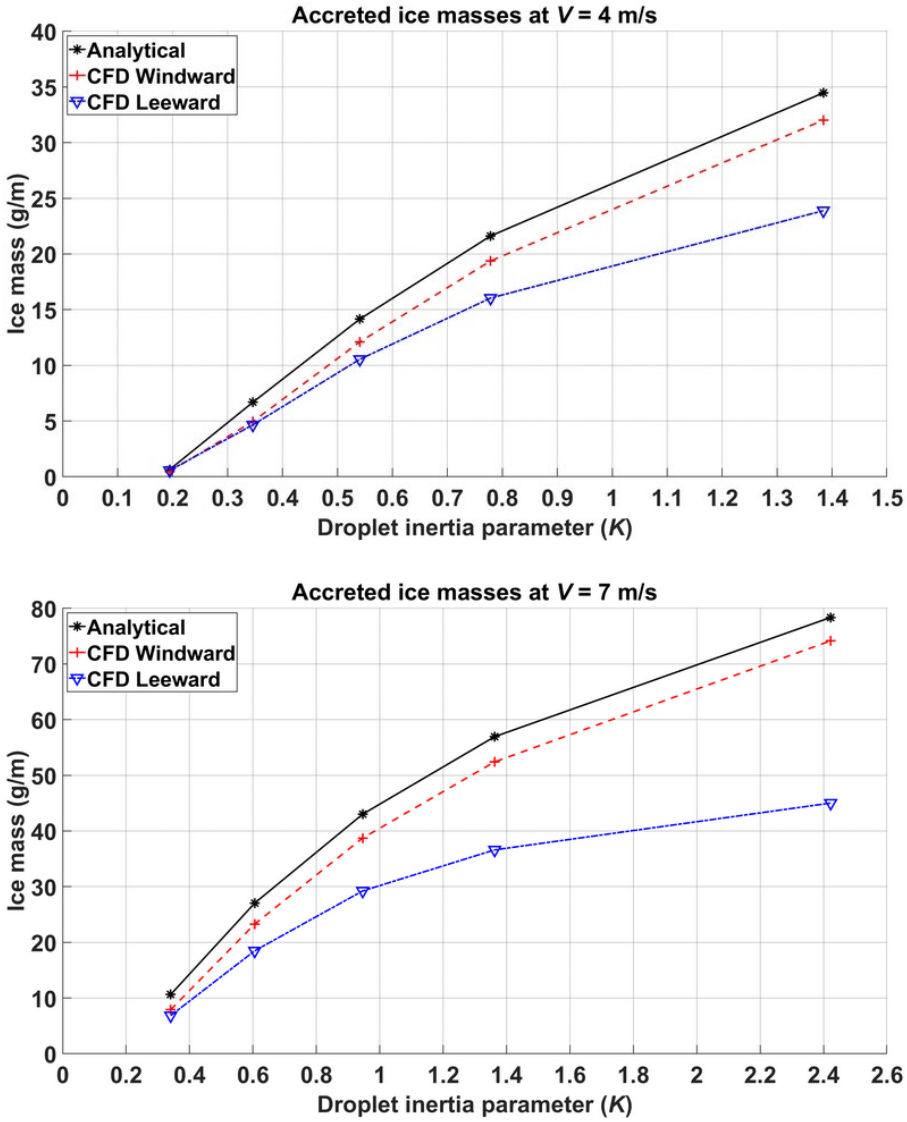

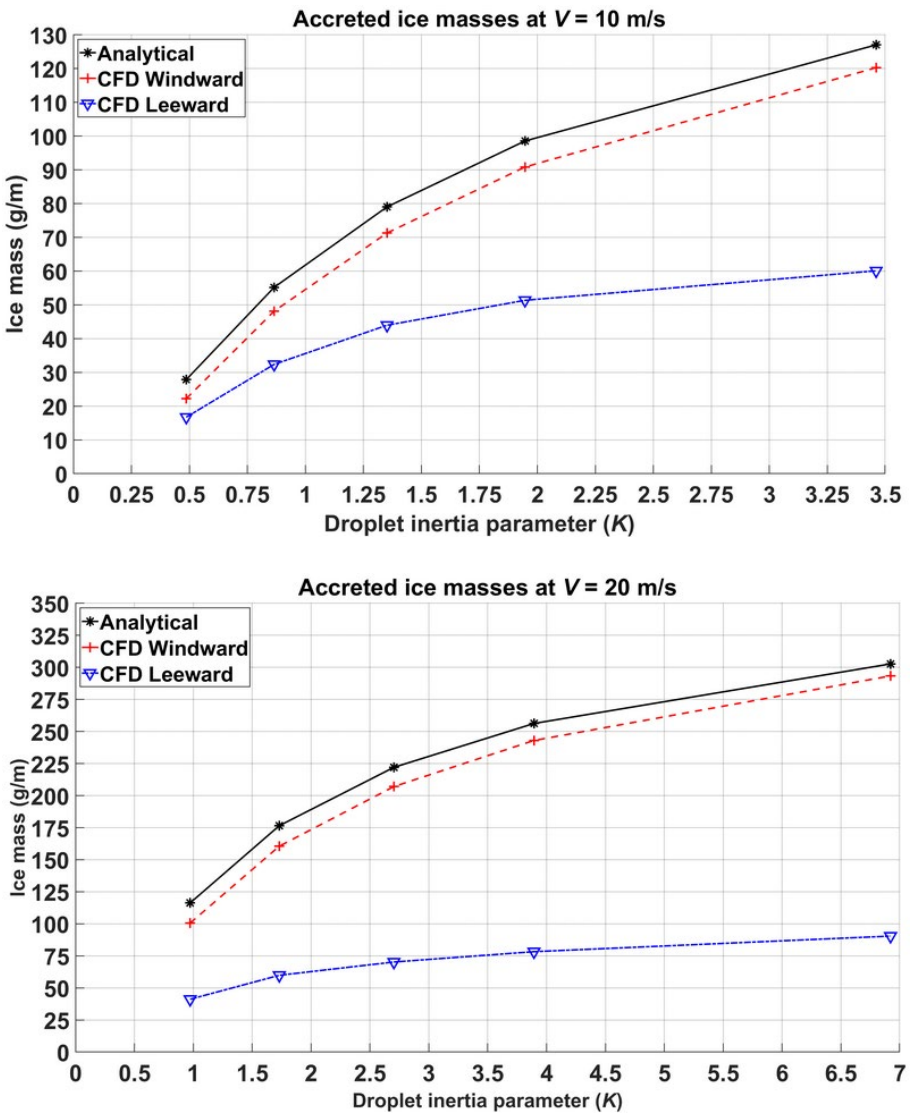

FIG. 13: Accreted ice masses vs. droplet inertia parameter K for different wind speeds. Each marker in the plot corresponds to one MVD from Table 4.

From Fig. 13 it can be seen that the analytical and the CFD results for the windward conductor agree well. On the contrary, the leeward conductor behaves rather differently from the windward conductor in CFD and analytical model, with an interesting tendency of "flat lining" in terms of accreted ice masses for the values of $K > 4$.

Having established the results for the ice accretion on the bundled cylinders at different

operating conditions for the 0° incidence angle, the results of the effect of the angle on the ice accretion on the bundled cylinders will be presented. For brevity, only one test case was selected from Table 2 for the purpose of studying the effect of the angle on the atmospheric ice accretion on the bundled cylinders. The selected test case has the MVD of 20 μm and the wind speed of 10 m/s. As with all cases the distance between cylinders is held constant at 500 mm and the desired angle is achieved by manipulating the horizontal and the vertical separation distances. The results from the ice accretion simulations on the angled bundle are given in terms of the overall collision efficiencies, their ratios and the accreted ice masses, and they are given in Table 7. As with all test cases in this study, the "dry growth" icing conditions are maintained, therefore, the accreted ice mass ratios are identical to the overall collision efficiencies ratios.

TABLE 7: Overall collision efficiencies, ratios and accreted ice masses on the angled cylinders

Vertical separation (mm)	Angle	Overall Collision Efficiency		Accreted Ice Mass (g/m)		Overall Collision Efficiency Ratio
		W	L	W	L	
15	1.7°	0.22	0.14	47.3	31.3	66%
30	3.4°	0.22	0.24	47.8	52.5	110%
60	6.8°	0.22	0.24	47.7	50.9	107%
129.4	15°	0.21	0.22	45.6	46.7	103%

Fig. 14 shows the distribution local collision efficiencies for the angled bundle configuration. For the dry growth conditions, the distribution local collision efficiencies are also representative of the accreted ice shapes.

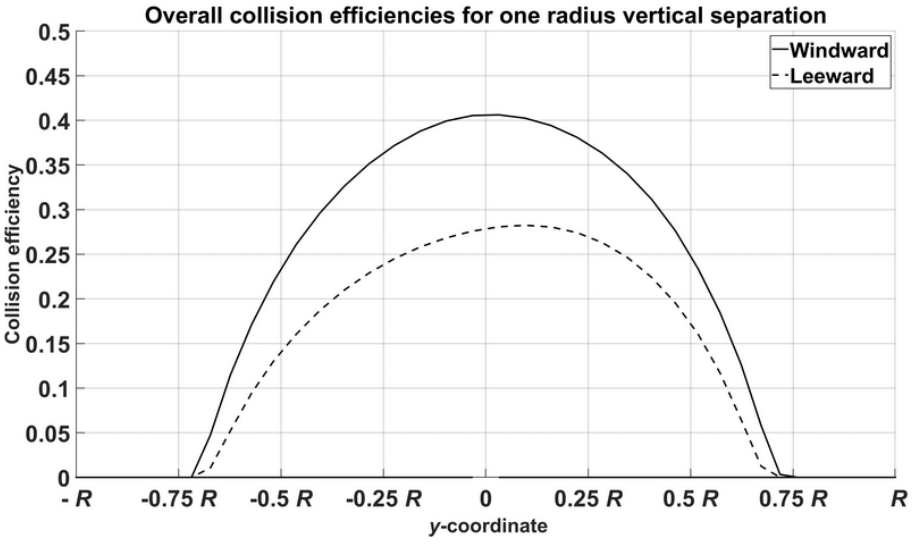
Overall collision efficiencies for one radius vertical separation
Windward
Leeward
Collision efficiency
0.5
0.45
0.4
0.35
0.3
0.25
0.2
0.15
0.1
0.05
0
- R
-0.75 R
-0.5 R
-0.25 R
0
0.25 R
0.5 R
0.75 R
R
y-coordinate

(a)

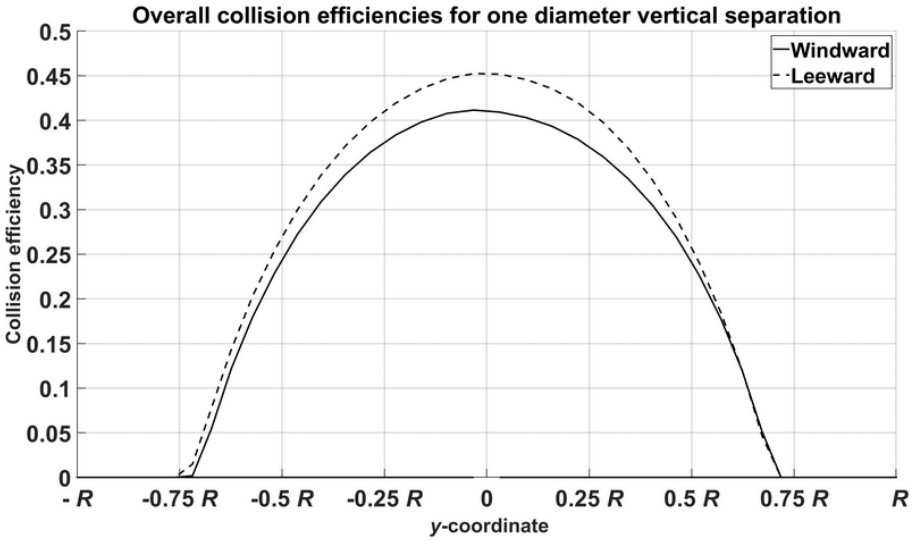
Overall collision efficiencies for one diameter vertical separation
Windward
Leeward
Collision efficiency
0.5
0.45
0.4
0.35
0.3
0.25
0.2
0.15
0.1
0.05
0
- R
-0.75 R
-0.5 R
-0.25 R
0
0.25 R
0.5 R
0.75 R
R
y-coordinate

(b)

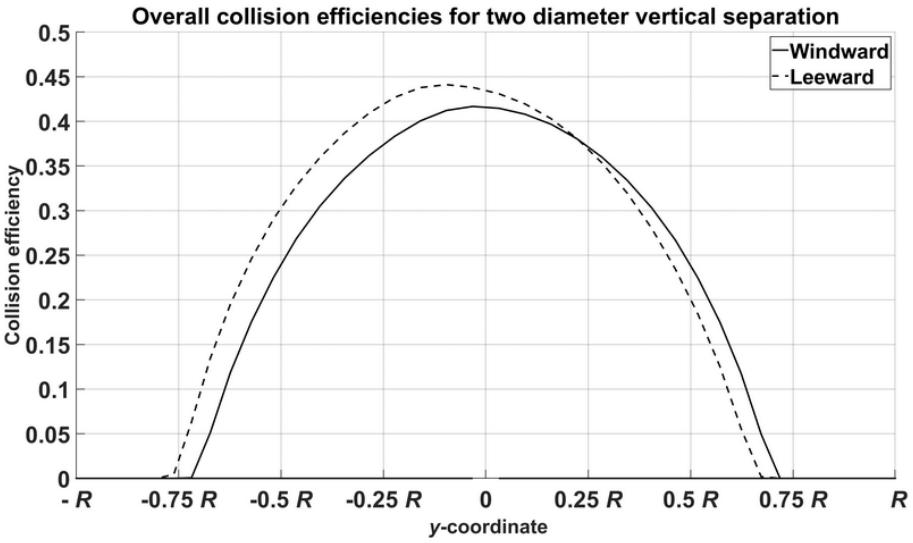
Overall collision efficiencies for two diameter vertical separation
Windward
Leeward
Collision efficiency
0.5
0.45
0.4
0.35
0.3
0.25
0.2
0.15
0.1
0.05
0
- R
-0.75 R
-0.5 R
-0.25 R
0
0.25 R
0.5 R
0.75 R
R
y-coordinate

(c)

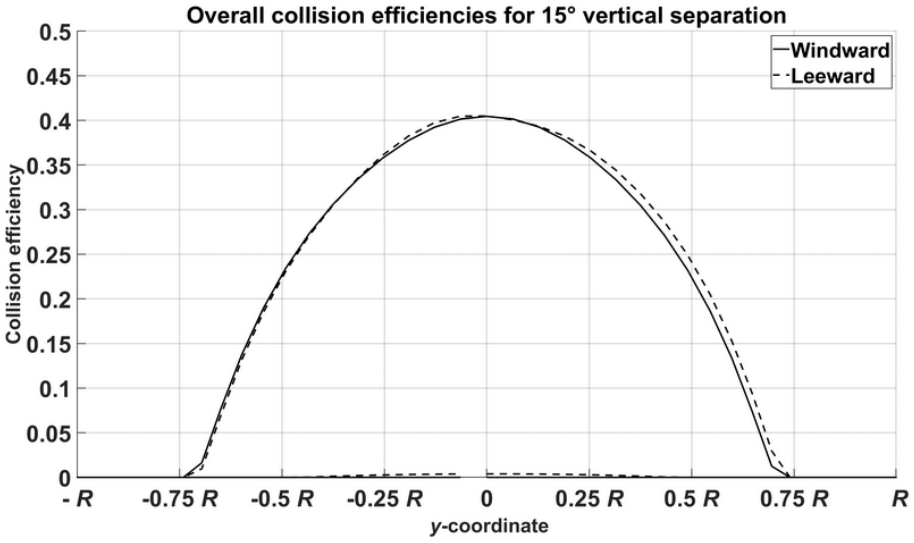

(d)

FIG. 14: Local collision efficiencies of the angled cylinders configuration. The vertical separations are 15 mm (one cylinder radius; a); 30 mm (one cylinder diameter; b); 60 mm (two cylinder diameters; c); and 129.4 mm, corresponding to the angle of 15° (d).

Fig. 15 shows the accreted ice masses and their ratios for the angled bundle configuration.

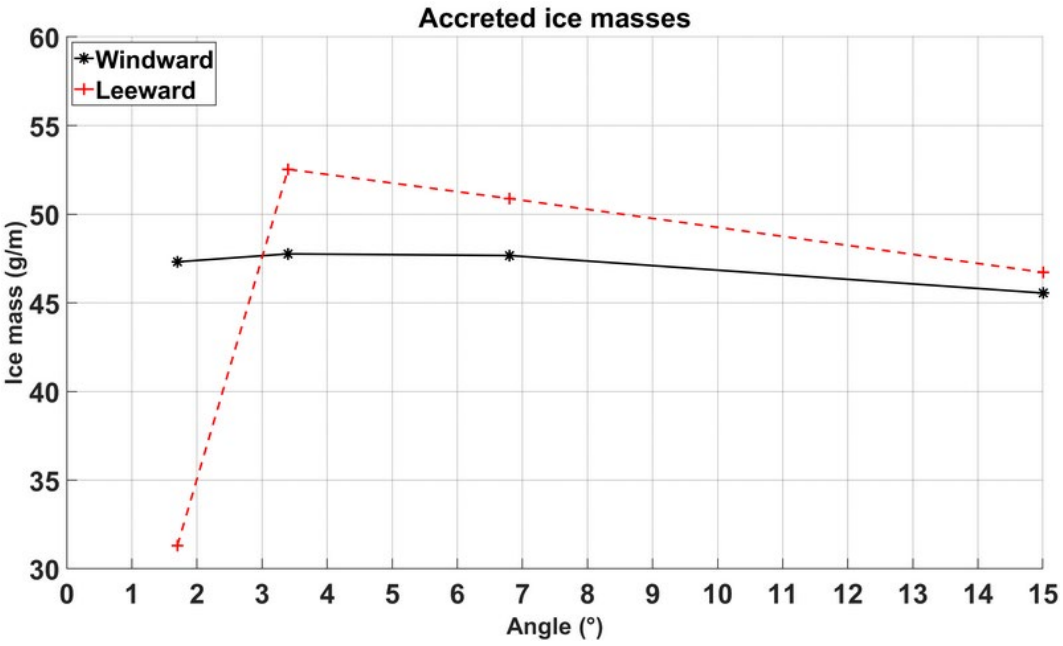

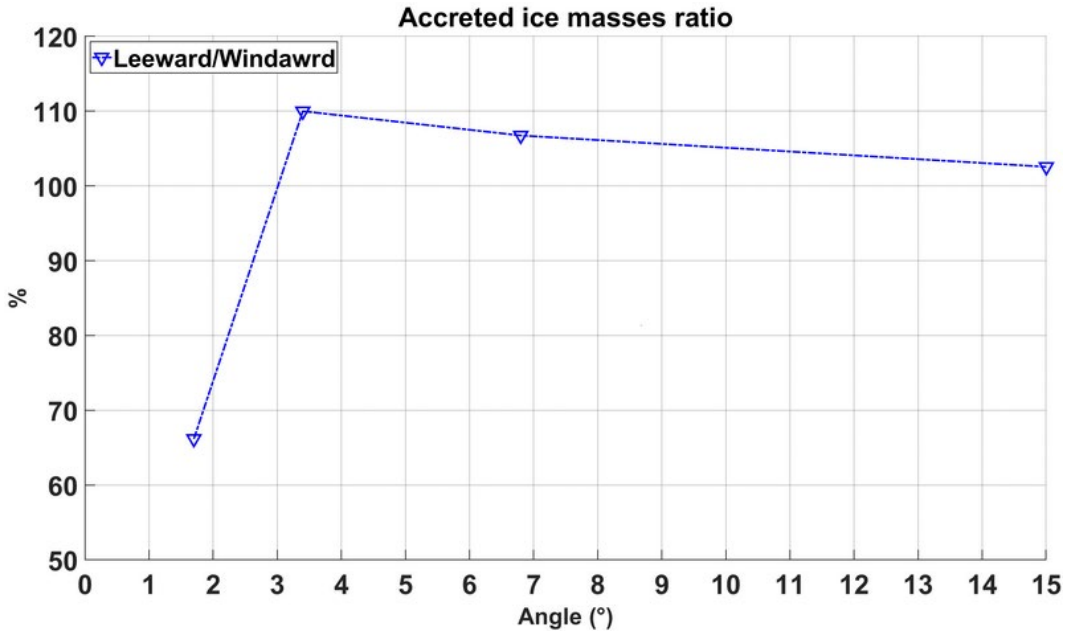

FIG. 15: Accreted ice masses (top) and their ratios (bottom) for the angled cylinders configuration

From the results in Table 6 and Figs. 14 and 15, it can be seen that at vertical separation of 15 mm, equal to the one cylinder radius, the "shielding" effects from the windward cylinder are very pronounced, limiting the amount of accumulated ice mass on the leeward cylinder at 67%, compared to the windward cylinder. This value is almost identical to the corresponding case from Table 4 simulated at 0° incidence. At the vertical separations of 30 and 60 mm, equal to the one and two cylinder diameters respectively, the ice accretion on the leeward cylinder "normalizes", becoming equal and even slightly higher than on the windward cylinder. This is more pronounced for the leeward conductor at one cylinder diameter vertical separation, which accretes approximately 10% more ice mass. This increased accretion can be explained by part of the multiphase flow, carrying significant LWC concentration at high speed being redirected from the top edge of windward cylinder onto the leeward one. The effect dissipates with the increase of vertical separation, as evidenced from the results at 15° angle, corresponding to the vertical separation of 129.4 mm which is slightly more than four cylinder diameters. In this case both

cylinders accrete almost identical ice masses, within 3% of each other.

These results tend to agree well with the ones from Wagner (2010), who notes that for the angle of twist of 1.91°, corresponding to the vertical separation of 13.33 mm, the leeward conductor accreted 86% ice mass, compared to the windward conductor. For the angle of 2.86° (vertical separation of 19.96 mm) the accreted ice mass ratio is almost 100%. However, some discrepancies between results of Wagner (2010) and this work are present. For the angle of 0.96° (6.7 mm), their leeward conductor accretes only 11% mass, and for the conductor at 0° Wagner writes that "*the downstream cable without any ice deposit*". Contrary, in this work the cable at 0° incidence accretes 67% ice mass. When comparing the operating conditions of Wagner (2010) with this work, the values of the droplet inertia parameter K and the Langmuir parameter φ are different, being $K = 0.87$ and $\varphi = 273.8$ for this work and $K = 1.27$ and $\varphi = 365.1$ in Wagner (2010), along with the ratio of the cylinder separation L to the diameter D. In this work $(L/D) = 16.67$ and for Wagner it is $(L/D) = 10$. The windward cylinders Reynolds number are 2.3×10^4 and 3.1×10^4, respectively.

The practical meaning of this phenomenon in the ice accretions on actual power lines with bundled conductors is, when the windward conductors accretes enough ice mass in order to sag sufficiently enough to no longer "shield" the leeward conductor, the ice accretions on the both conductors in the bundle will be almost equal and thus they can be modeled using simplex configuration in CFD along with the formulae of ISO 12494, if desired. This does not take into account the possibility and potential implications of vibrations or rotations of the conductors, due to fluid-structure interaction. It is assumed that these interactions can cause the windward conductor to no longer "shield" the leeward conductor at even earlier point in time during an icing event. However, these potential effects are not within the focus of current study and will

not be ascertained here.

5. ICING TUNNEL EXPERIMENTS

For the validation of the numerical model and obtained results in this study the ice accretion values from the duplex cylinders in the icing wind tunnel are used. This experimental distribution is imported using a “Custom Distribution” option within the DROP3D. As the VTT experimental distribution is provided in terms of bin with prescribed bounds, and the DROP3D expects the MVD value of the bin, the MVD value of each bin is calculated first, and then used in the “Custom Distribution” function. The LWC content of each bin is imported as-is. The operating conditions in the icing wind tunnel are similar of these in Table 1 with exceptions of wind speed being 4 m/s and instead of monodispersed distribution with MVD of 20 μm, the actual experimental droplet distribution spectrum is used in numerical simulations. This experimental distribution is given in Fig. 16 and Table 8.

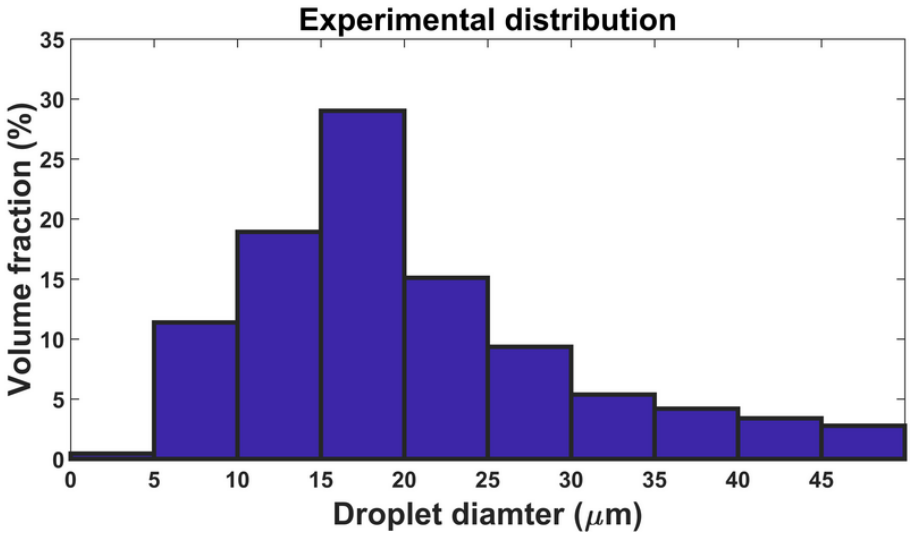

FIG. 16: Experimental distribution

TABLE 8: Experimental distribution

Bin (μm)	Bounds (μm)	LWC fraction
5	0.61 – 5	0.0045
10	5 – 10	0.1138
15	10 – 15	0.1893
20	15 – 20	0.2902
25	20 – 25	0.1510
30	25 – 30	0.0935
35	30 – 35	0.0537
40	35 – 40	0.0419
45	40 – 45	0.0339
50	45 – 50	0.0277

The experiments were conducted in the VTT Technical Research Centre of Finland icing wind tunnel. This is an "open-loop" tunnel placed entirely inside a large cold room. The cross-section of the tunnel mouth is 0.7 m by 0.7 m. Ice was grown on 0.5 m long smooth aluminum cylinders, 30 mm in diameter, placed vertically close to the center of the tunnel. The schematic of the icing wind tunnel is given in Fig. 17. To rule out the effect of blockage, the cylinders were located in front of the exit of the tunnel. The temperature and wind speed in the test section were measured using calibrated sensors. The liquid water content (LWC) was calibrated for each wind speed and temperature pair by measuring the ice growth on a 30 mm cylinder and using the formulas defined in ISO 12494 (ISO, 2001). Under the test conditions, LWC was 0.4 g/m^3. The air temperature was –5 °C and wind speed 4 m/s. The droplet size distribution in the icing tunnel has been calibrated by using The Cloud, Aerosol and Precipitation Spectrometer probe (CAPS), which can measure small particles between 0.61 and 50 μm by utilizing the light scattering principle. The calculated MVD of this distribution is 18.73 μm.

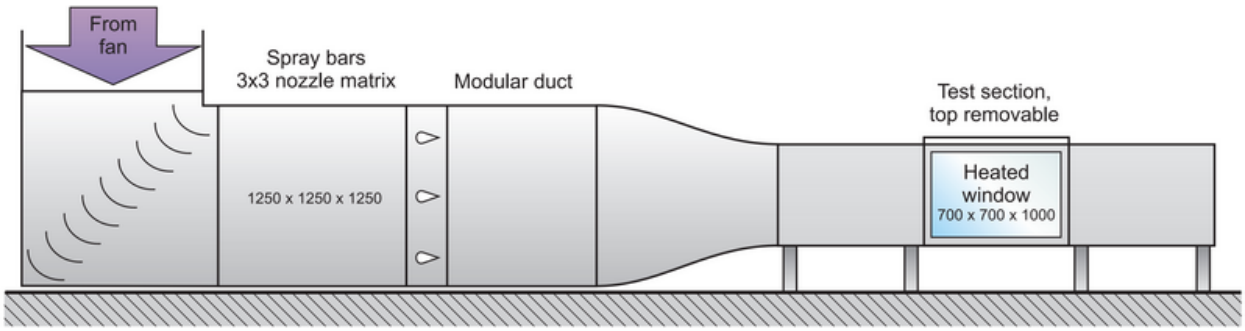

FIG. 17: Icing wind tunnel schematic (Jokela and Prieto, 2020)

An example of ice shape obtained from the icing tunnel experiments is shown in Fig. 18. Do note that during the icing experiments that the information about the circumferential icing distribution was not measured during experiment, except the end ice shapes were measured/photographed.

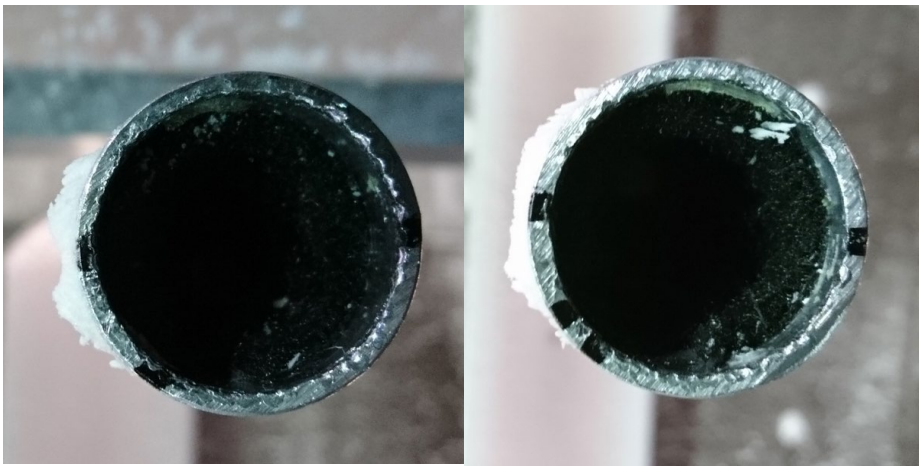

FIG. 18: Sample ice accretion shapes in the icing wind tunnel for the windward (left) and leeward (right) cylinders

Table 9 lists the comparison of numerical simulation results compared to the experimental values.

TABLE 9: Overall collision efficiencies, accreted ice masses and ratios in experimental vs. numerical results

Test case	Wind speed (m/s)	Overall Collision Efficiency		Accreted Ice Mass (g)		Ice Masses Ratio
		W	L	W	L	
Experiment	4	0.12	0.09	5.1	3.9	77%
CFD Spectrum		0.10	0.08	4.2	3.3	79%
CFD Monodispersed		0.04	0.04	1.6	1.6	100%
Experiment	7	0.23	0.17	17.5	12.6	72%
CFD Spectrum		0.17	0.12	13.0	9.3	72%
CFD Monodispersed		0.13	0.10	9.6	7.8	81%
Experiment	10	0.22	0.17	23.7	18.6	78%
CFD Spectrum		0.23	0.14	24.5	14.9	61%
CFD Monodispersed		0.19	0.13	20.8	14.3	69%
Experiment	20	0.38	0.23	82.9	50.4	61%
CFD Spectrum		0.35	0.11	75.7	22.8	30%
CFD Monodispersed		0.34	0.13	73.3	28.8	39%

Visually, the results from Table 9 are also given in Figs. 19 and 20 in a graphical form.

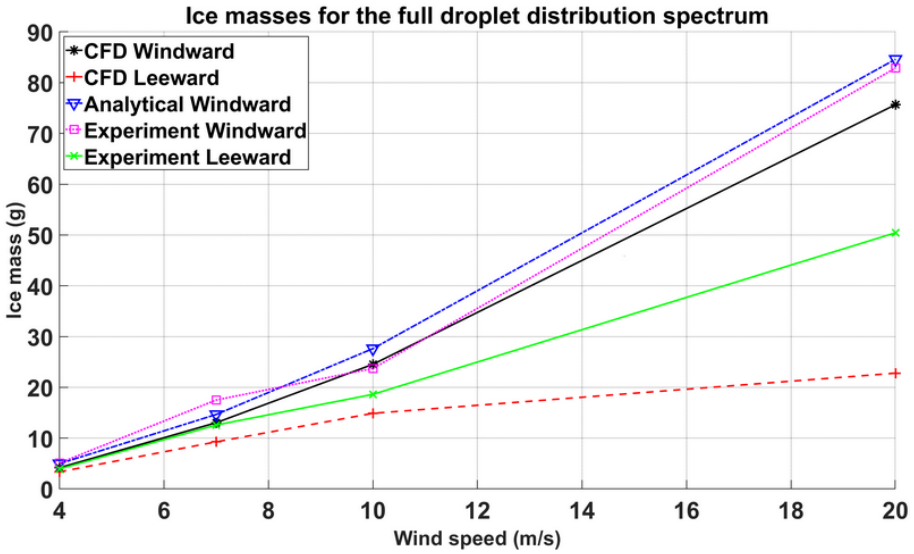

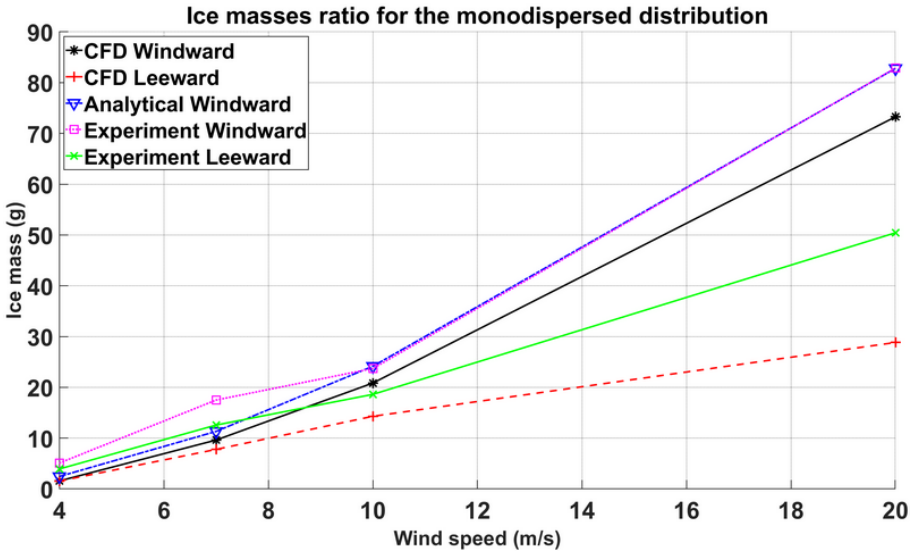

FIG. 19: Accreted ice masses for the full droplet distribution spectrum (top) and monodispersed distribution (bottom)

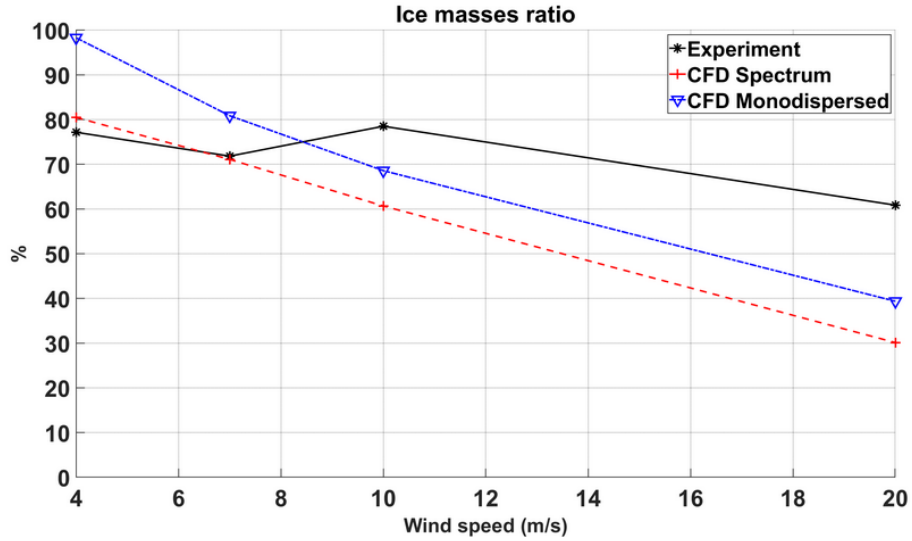

FIG. 20: Accreted ice masses ratio

From the values in Table 9 and Figs. 19 and 20 it can be seen that the CFD simulations results tend to underestimate the values of accreted ice masses and overall collision efficiencies, in particular on the leeward cylinder at 20 m/s wind speed. The accreted ice masses ratio in the CFD simulations has good agreement with the experimental values, for the 4 and 7 m/s wind speed conditions, acceptable agreement for the 10 m/s wind speed conditions (keeping in mind

the apparent increase in the accreted ice masses ratio at this wind speed, as seen from Fig. 19) and rather poor agreement at 20 m/s wind speeds.

The possible reason for underperformance of the CFD model at 10 and 20 m/s wind speeds, when compared to the experimental values is twofold. First, Qing et al. (2018) do not have the experimental data point, corresponding to the 500 mm cylinder separation. The "experimental value" presented in this study is taken as average value between Qing et al (2018) results at 400 and 600 mm cylinder separation. Second, is the "attachment" of the "end plate" of the bundled cylinders during their wind tunnel experiments, and its potential effects on the airflow conditions during the experiments.

In addition, the ratio of the overall collision efficiencies lines up with the previously established trend from Table 4, where the decrease in the operating wind speed and/or the value of MVD leads to the increase in the overall collision efficiencies ratios between the leeward and the windward cylinders. Overall, the agreement between the CFD simulation results and the experimental values is acceptable. Furthermore, the results with MVD approximation in Fig. 20 consistently given the higher accreted ice mass ratio, than the results with the full droplet distribution spectrum. Similarly, the primary reason behind this is the high sensitivity of the spectrum averaged results to the largest droplet sizes in the distribution and the tendency of decreasing of the accreted ice masses ratio with the increase in the values of the droplet inertia parameter K, with the larger droplets obviously possessing higher values of K. This scaling is highly non-linear as the droplet inertia parameter scales with the droplet size d as a factor d^2. Then, in the numerical model, the droplet inertia parameter K comes in the droplet's equation of motion as shown in the eqs. (14) and (15) in this work, which do have an exponential scaling with the droplet drag coefficient Re_d. In practical terms, it means that the larger droplets in the

spectrum, have higher values of the droplet inertia parameter K and are thus the primary factor "responsible" for the majority of the ice accretion from the spectrum. However, by increasing the K value further, the collision efficiencies of the larger droplets will not increase in "linear" fashion with K, as its highly likely that they already have the collision efficiency close enough to the physical limit of unity, i.e., close to all impinging large droplets collide with the object. However, in the MVD approximation, all droplets have the same, uniform size, thus by increasing their K in the limit of high inertia, the corresponding increase in the collision efficiency values will be higher. This mathematical phenomena is fully inline with the discussions of (Langmuir and Blodgett, 1946) who first observed this mathematical behavior of droplet distribution spectra when compared to the monodispersed distribution in their work.

Fig. 21 illustrates this concept in more details, showing per bin overall collision efficiencies ratio of the experimental distribution under experimental operating conditions.

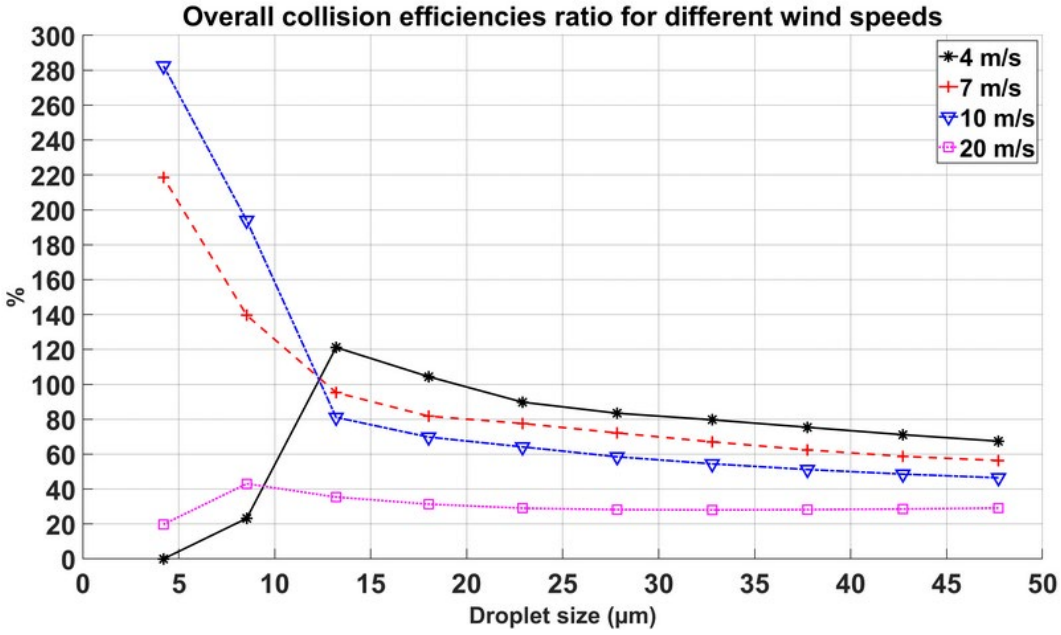

FIG. 21: Per bin overall collision efficiencies ratio

Disregarding some cases of the overall collision efficiencies ratio being significantly in excess of 100% (same arguments as with the test case at V = 4 m/s with MVD = 15 μm and the resultant value of K can be made) and possible lack of physical meaning of it (for those smaller droplet sizes the overall collision efficiencies are of an order of less than 0.01), the overall trend is clear. The overall collision efficiencies ratio of the larger droplet sizes, for example 40–50 μm is significantly lower than the ratio for the smaller bins, e.g. 20 – 25 μm. Since the monodispersed distribution contains only one droplet size in it, the results for it are not being affected in the similar fashion.

6. CONCLUSION

Within this work a series of CFD simulations have been performed on the bundled cylinders under the dry ice growth regime. The primary interest of modeling of such geometric configurations comes from the need of modeling the ice accretion on bundled conductors on the power lines. First, is to "fill the gaps" in the works of Wagner (2010) and Qing et al. (2018), mostly, in an attempt to "expand" the work by Wagner (2010), by presenting the accreted ice mass ratios for the simulations within this study, in attempt to further quantify the "partial ice accretion on downstream conductor" statement. Second, is to ascertain the viability of the commercial CFD package in the modeling of the dry ice accretion on the bundled conductor, as opposed to creating the in-house code. If such ice accretions can be viably modeled by a commercial CFD software, then it would be readily possible to extend this work further, in an attempt to produce the accreted ice masses ratio between the windward and the leeward conductor as a function of the operating conditions.

For this purpose, a circular cylinder is considered an acceptable approximation. The

performed simulations cover a wide range of possible icing conditions by varying the operating wind speed, from 4 to 20 m/s and MVDs from 15 to 40 μm respectively. The obtained results for the 0° angle of incidence show that the overall collision efficiencies and accreted ice mass ratios between the leeward and the windward cylinders varies from ~100% to ~30%. This ratio decreases with the increase in the values of the operating wind speed and/or median volume diameter. This can be explained by the increase in the droplet inertia, corresponding to the increase of droplet's inertia parameter K, as a function of droplet's size and wind speed. Specifically, with the increase in the operating wind speed, the droplets have less "window time" to adapt to the flow conditions past the windward conductor and move into a trajectory which allows a collision with the leeward cylinder.

For the comparison with the experimental data, the CFD simulations have a good agreement in terms of the accreted ice masses ratio for the 4 and 7 m/s wind speed conditions, acceptable agreement at 10 m/s wind speed and rather poor agreement at 20 m/s. There are a few potential explanations for this poor agreement at specifically this wind speed. The primary factor are the changes in the wake behavior at this wind speed, with the significant vortex shedding present. As a result, a significant portion of the droplets is entrained in the said vortices. Other possible explanations include the larger wake, and its influence on the leeward conductor, as predicted by the $k - \omega$ model when compared to the $k - \varepsilon$ model, as discussed in Wagner (2010). Finally, it may also come to the deficiency of the experimental setup of Qing et al. (2018) as the cylinders in it were fixated by rather large top plate, as shown in Fig. 22. The potential effect of this plate on the behavior of the multiphase flow, and as a result – the accreted ice and their masses was not studied by original authors.

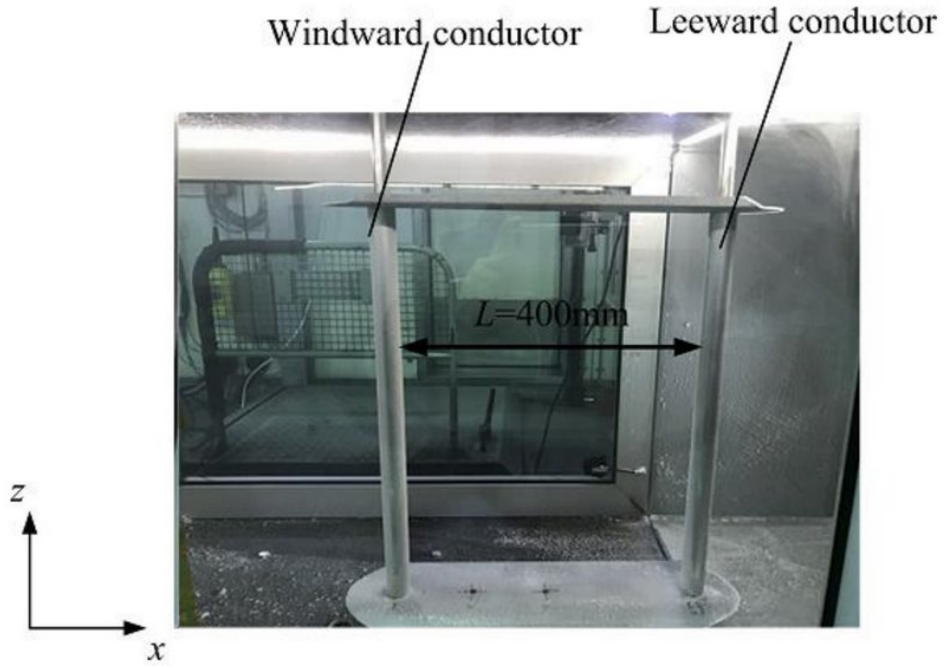

FIG. 22: Top plate in the icing wind tunnel experiments of Qing et al. (2018)

Overall, the CFD simulations tend to underestimate the accreted ice masses in the experiment, to an extent, particularly, for the monodispersed distribution, and the monodispersed distribution consistently shows the higher ratio of the accreted ice masses. This "feature" is believed to be again the primary impact of the droplet inertia parameter K on the accreted ice masses ratio. In the full droplet distribution spectrum, the "spectrum-average" results depend significantly on the larger droplets in the spectrum, which, by the nature of them being of the larger diameter, have higher value of K, when compared to the rest of the droplet sizes and/or the monodispersed distribution. The monodispersed distribution, featuring only one droplet size, is lacking this "feature".

For a case of bundled cylinders at 10 m/s wind speed and 20 μm MVD, the angle of incidence was varied from 0° to 15°, and angles corresponding to the vertical separations being equal to one cylinder radius and one and two cylinder diameters, respectively. This was primarily

done in order to ascertain the effects of an angle and potential sag due to accreted ice on the power line. For the cases with non-zero angle of incidence, the simulated overall collision efficiencies and accreted ice masses are approximately equal, with the leeward cylinder accreting slightly more ice, as soon as the angle of incidence is large enough to introduce a vertical separation equal or greater of one cylinder diameter. This can be explained by leeward cylinder being no longer "shielded" by the windward one and thus the effects of perturbed airflow past the windward cylinder are no longer significantly affect the leeward cylinder. In such cases it is deemed possible to model the resulting ice accretion on the bundled cylinders using simplex configuration and ISO 12494 analytical modeling framework.

ACKNOWLEDGMENTS

The work reported in this paper is funded by the Research Council of Norway, nICE - project no. 324156 & IceBOX – project no. 282403. Authors would like to acknowledge Mr. Timo Karlsson and Mr. Miko Tiihonen from VTT for providing icing wind tunnel experimental data used in this research work.

The Authors declare that there is no conflict of interest.

REFERENCES

Beard, K.V. and Pruppacher, H.R., A Determination of the Terminal Velocity and Drag of Small Water Drops by Means of a Wind Tunnel, *J. Atmos. Sci.*, vol. **26**, pp. 1066–1072, 1969. DOI: 10.1175/1520-0469(1969)026<1066:ADOTTV>2.0.CO;2

Bourgault, Y., Habashi, W.G., Dompierre, J., and Baruzzi, G.S., A Finite Element Method Study of Eulerian Droplets Impingement Models, *Int. J. Numer. Methods Fluids*, vol. **29**, pp. 429–449,

1999.

Finstad, K.J., Numerical and Experimental Studies of Rime Ice Accretion on Cylinders and Airfoils, PhD, University of Alberta, 1986. DOI: 10.7939/R3N58CS1V

Finstad, K.J., Lozowski, E.P., and Gates, E.M., A Computational Investigation of Water Droplet Trajectories, *J. Atmos. Ocean. Technol.*, vol. **5**, pp. 160–170, 1988. DOI: 10.1175/1520-0426(1988)005<0160:ACIOWD>2.0.CO;2

ISO, International Organization for Standardization, Atmospheric Icing of Structures, ISO Standard 12494:2001(E), Geneva, Switzerland, 2001.

Jokela, T. and Prieto, R., Wind Power Icing Wind Tunnel, accessed October 12, 2022, from https://www.vttresearch.com/sites/default/files/2020-06/Wind%20power_Icing_wind_tunnel.pdf, 2020.

Lam, C.K.G. and Bremhorst, K., A Modified Form of the $k - \varepsilon$ Model for Predicting Wall Turbulence, *J. Fluid Eng.*, vol. **103**, pp. 456–460, 1981.

Langmuir, I. and Blodgett, K., A Mathematical Investigation of Water Droplet Trajectories, Army Air Forces Headquarters, Air Technical Service Command, Army Air Forces Tech. Rep. 5418, 1946.

Lozowski, E.P. and Makkonen, L., Fifty Years of Progress in Modelling the Accumulation of Atmospheric Ice on Power Network Equipment, *Proc. of the 11th Int. Workshop on Atmospheric Icing of Structures*, Montreal, Canada, 2005.

Makkonen, L., Modeling of Ice Accretion on Wires, *J. Appl. Meteorol.*, vol. **23**, pp. 929-939, 1984. DOI: 10.1175/1520-0450(1984)023<0929:MOIAOW>2.0.CO;2

Makkonen, L. and Stallabrass, J.R., Experiments on the Cloud Droplet Collision Efficiency of Cylinders, *J. Appl. Meteorol.*, vol. **26**, pp. 1406–1411, 1987.

Menter, F.R., Improved Two-Equation k – ω Turbulence Models for Aerodynamic Flows, National Aeronautics and Space Administration, Ames Research Center, NASA Technical Memorandum 103975, 1992.

Morsi, S.A. and Alexander, A.J., An Investigation of Particle Trajectories in Two-Phase Flow Systems, *J. Fluid Mech.*, vol. **55**, pp. 193–208, 1972. DOI: 10.1017/S0022112072001806

Papadakis, M., Wong, S.-C., and Rachman, A., Large and Small Droplet Impingement Data on Airfoils and Two Simulated Ice Shapes, National Aeronautics and Space Administration, Glenn Research Center, NASA/TM—2007-213959, October 2007.

Qing, H., Jian, Z., Mengyan, D., Dongmei., D. Makkonen, L., and Tiihonen, M., Rime Icing on Bundled Conductors, *Cold Regions Sci. Technol.*, vol. **158**, pp. 230–236, 2018.

Ratvasky, T.P., Barnhart, B.P., and Lee, S., Current Methods for Modeling and Simulating Icing Effects on Aircraft Performance, Stability and Control, National Aeronautics and Space Administration, Glenn Research Center, NASA/TM—2008-215453, AIAA–2008–6204, December 2008.

Schmidt, R.C. and Patankar, S.V., Two-Equation Low-Reynolds-Number Turbulence Modeling of Transitional Boundary Layer Flows Characteristic of Gas Turbine Blades, National Aeronautics and Space Administration, Lewis Research Center, NASA Contractor Report 4145, May 1988.

Veerakumar, R., Tian, L., Hu, H., and Hu, H., An Experimental Study of Atmospheric Icing Process on Bundled Conductors, *Proc. – 19th Int. Workshop on Atmospheric Icing of Structures*, Montreal, Canada, 2022.

Wagner, T., Modelling of Wind-Borne Ice Accretion on Power Transmission Lines, PhD, University of Braunschweig, 2010.

White, F.M., *Fluid Mechanics 5th Edition*, New York: McGraw-Hill, 2002.

Wiberg, B.D., Fujiwara, G.E.C., Woodard, B.S., and Bragg, M.B., Large-Scale, Swept-Wing Icing Simulations in the NASA Glenn Icing Research Tunnel Using LEWICE3D, *6th AIAA Atmospheric and Space Environments Conf.*, Atlanta, GA, 2014. DOI: 10.2514/6.2014-2617